

Mechanical anisotropy of 3D-printed digital materials at large strains

Seunghwan Lee¹, Gisoo Lee², Seounghee Yun¹, Sumin Lee², Jeonyoon Lee², Hansoel Cho^{1†}

¹Department of Mechanical Engineering, ²Department of Aerospace Engineering, Korea Advanced Institute of Science and Technology, Daejeon, 34141, Republic of Korea

E-mail: [†]hansoel@kaist.ac.kr

Abstract. 3D-printed digital materials whose mechanical behavior travels between those from thermoplastic to rubbery polymers have become increasingly important. However, their mechanical functionalities have not been fully exploited due to intrinsic mechanical anisotropy resulting from microstructural heterogeneity. Here, we combine mechanical testing, microscopy analysis and micromechanical modeling for a comprehensive understanding of complex deformation mechanisms responsible for the printing-orientation-dependent nonlinear mechanical behavior of digital materials at small to large strains. Towards this end, we construct representative volume elements that account for highly anisotropic microstructural features resulting from the printing-orientation-dependent diffusion and mixing between photocurable base resins. We then demonstrate, through micromechanical analysis, that stable compressive deformation of well-aligned elliptical hard thermoplastic inclusions embedded within the surrounding soft rubbery matrix gives rise to initial elastic anisotropy. Our experimental and micromechanical modeling results also show that the interplay between buckling instability and plastic deformation of the high-aspect-ratio hard domains governs mechanical anisotropy at large strains as well as the printing-orientation-dependent resilience and energy dissipation capabilities in these digital materials.

1 Introduction

Understanding processing-microstructure-property relationships is of critical importance in three-dimensional (3D) printing (Gibson et al. 2021; Gu et al. 2021; Park et al. 2022). It has become increasingly important with the growing interest in multi-material printing (Zhu et al. 2024; Brown et al. 2025) as well as in metal additive manufacturing (Sames et al. 2016; Gu et al. 2021). More specifically, the microstructural heterogeneities that form during these printing processes play a central role in the emergence of printing-orientation-dependent mechanical properties in additively manufactured materials and components (Martin et al. 2017; Raney et al. 2018; DebRoy et al. 2018; Telles et al. 2025). However, a comprehensive mechanistic un-

derstanding of the microstructural mechanisms governing mechanical anisotropy in additively manufactured materials remains elusive, especially under large deformation. This is primarily attributed not only to experimental difficulties associated with direct measurements of local mechanical properties at the length scales of the printed microstructures but also due to the coupling between multiple microscopic deformation mechanisms.

Material jetting offers the distinctive capability of simultaneously depositing multiple materials with high precision, as widely demonstrated by both commercial (e.g., Stratasys and 3D Systems; Inkbit and Mimaki) and customized (e.g., Sitthi-Amorn et al. 2015; Roach et al. 2019; Buchner et al. 2023) multi-material printers. This is achieved by rapidly solidifying microscale liquid resins through photopolymerization upon UV exposure (Ligon-Auer et al. 2016; Park et al. 2022). In particular, multi-material jetting processes enable the precise fabrication of “digital materials” by depositing hard and soft photocurable base resins at prescribed spatial locations. Varying the mixing ratio of these base resins allows digital materials to exhibit hybrid mechanical properties between thermoplastic and rubbery polymers. Over the past decade, digital materials whose mechanical behaviors show thermoplastic to rubbery features (e.g., Yi et al. 2006; Deschanel et al. 2009; Cho et al. 2013a; Cho et al. 2013b; Cho et al. 2017; Lee et al. 2023b) have been widely employed to fabricate physical prototypes for a wide range of applications. Examples include mechanically (Zhao et al. 2025), thermally (Wu et al. 2016; Li et al. 2023), chemically (Mao et al. 2016), and electromagnetically (Akbari et al. 2019) responsive materials and devices. The printing of digital materials has also been widely used in the areas of soft robotics and actuation (Bartlett et al. 2015; Wang et al. 2017). Recently, it has enabled the design and manufacture of heterogeneous or cellular architected materials that exhibit unusual mechanical functionalities (Cho et al. 2016; Liu and Li 2018; Fernandes et al. 2021; Reyes-Martinez et al. 2022; Lee et al. 2024a).

In parallel, the deformation and failure of these digital materials have been characterized through mechanical testing (Wu et al. 2016; Akbari et al. 2019; Zorzetto et al. 2020; Abu-Qbeidah et al. 2025) and continuum-based constitutive modeling (Slesarenko and Rudykh 2018; Xiang et al. 2019; Lee et al. 2024a; Moon et al. 2025). More recently, physics-augmented neural networks have been utilized to gain a better understanding of the deformation mechanisms in these materials, which often encompass significant microstructural uncertainties (Yang et al. 2025; Klein et al. 2026). It should also be noted that the base materials have been widely reported to exhibit nearly isotropic mechanical behavior from small to large strains (Zhang

and To 2016; Zerhouni et al. 2019; Lee et al. 2024b). However, digital materials for which two base resins are deposited together have been shown to exhibit significantly orientation-dependent elastic stiffness, plastic strength and fracture toughness (Bass et al. 2016; Lumpe et al. 2019; Ituarte et al. 2019). Furthermore, optical microscopy observations have revealed highly anisotropic microstructures characterized by well-aligned and elongated hard inclusions embedded within the soft surrounding matrix, or *vice versa* (Mueller et al. 2017; Zorzetto et al. 2020). These observations further highlight the need to gain a fundamental understanding of mechanical anisotropy in these 3D-printed digital materials, which would be essential to exploit their potential fully in a wide range of engineering applications.

In this work, by combining mechanical experiments, microscopy analysis and micromechanical modeling, we address the microstructural mechanisms that govern the printing-orientation-dependent mechanical behavior of digital materials fabricated using a high-resolution multi-material 3D printer (Connex3 Objet260, Stratasys Inc.). To this end, we construct representative volume elements (RVEs) that capture the key microstructural features observed in optical microscopy images of digital materials, where elliptical hard domains with high aspect ratios are well aligned within the surrounding soft matrix. Through micromechanical analysis, we demonstrate that high-aspect-ratio elliptical hard inclusions give rise to the initial elastic anisotropy. More importantly, our micromechanical modeling results reveal that the interplay between buckling instability and plastic deformation in elliptical hard domains connected along the printing direction governs the significant mechanical anisotropy in digital materials under large strains. The influence of the stiffness ratio between hard and soft domains is further explored to examine the orientation-dependent mechanical resilience and energy dissipation under loading and unloading conditions. Quantitative agreement is found between experimental and micromechanical modeling results, demonstrating that the approach presented in this work can advance our understanding of the printing-orientation-dependent mechanical behaviors observed in multi-material, 3D-printed digital materials.

The paper is organized as follows. The printing-orientation-dependent large-strain mechanical behavior of representative 3D-printed digital materials is presented in Section 2. We then investigate the microstructural features of the digital materials through optical microscopy analysis in Section 3 and Appendix A. A facile procedure to construct representative volume elements that mimic the realistic hard and soft microstructures observed in digital materials is then presented in Section 4. Furthermore, we compare the micromechanical modeling results

with the corresponding experimental data, by which we demonstrate that well-aligned elliptical hard inclusions play a crucial role in the mechanical anisotropy in these digital materials under small to large strain levels. We then discuss further implications of the micromechanical modeling results on the mechanical resilience and energy dissipation capabilities of these digital materials in Section 5. We close the paper by summarizing the main findings in Section 6. Detailed information on the constitutive models used in the hard and soft components in the micromechanical analysis is presented in Appendix B. Additional micromechanical modeling results of the digital materials are provided in Appendix C.

2 Mechanical anisotropy at small to large strains

The orientation-dependent mechanical behavior of 3D-printed, digital materials is examined under large strain loading and unloading conditions. To this end, we selected two base materials,

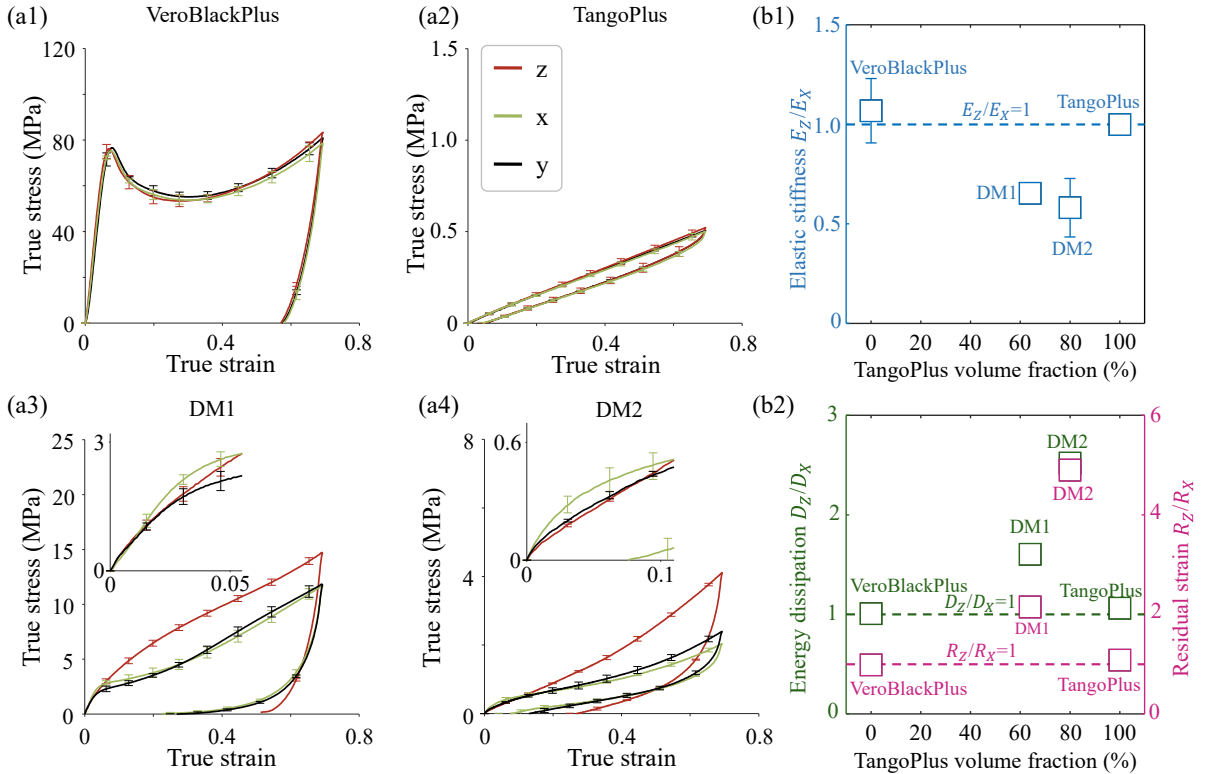


Figure 1: Printing-orientation-dependent mechanical behavior of 3D-printed materials. Stress-strain curves of (a1) and (a2) base materials (VeroBlackPlus and TangoPlus) and (a3) and (a4) digital materials (DM1 and DM2) printed in the x-, y- and z-directions during loading and unloading at a strain rate of 0.01 s^{-1} (insets: printing-orientation-dependent stress-strain curves of the DM1 and DM2 materials at small strains). (b1) Ratios of elastic stiffnesses and (b2) ratios of energy dissipations and residual strains in the digital materials printed in the z- and x-directions.

VeroBlackPlusTM (hard) and TangoPlusTM (soft), and their mixtures (i.e., digital materials) with Shore A hardness (Stratasys 2021) of 95 and 70 (labeled DM1 and DM2 in this work). For each material, cylindrical specimens with a diameter of 10 mm and a height of 5 mm were printed in three different directions, each defined such that the axis of the global coordinate system (x, y, z) was aligned with the longitudinal axis of the cylindrical specimen. In this work, the global x - and z -axes were set to be the printing direction and the deposition direction of the sequential layers, respectively. After removing the support material (SUP705BTM) through manual brushing, the 3D-printed specimens were kept under ambient conditions for approximately 24 hours. We then conducted uniaxial compression tests on these specimens at a strain rate of 0.01 s^{-1} using a universal mechanical testing machine (INSTRON 4482) at room temperature (295K). Figure 1 presents the printing-orientation-dependent stress-strain curves of the base materials (VeroBlackPlus and TangoPlus) and the digital materials (DM1 and DM2). As shown in Figures 1a1 and 1a2, the base materials were found to be nearly isotropic at small to large strains. The hard VeroBlackPlus material exhibits standard thermoplastic polymeric behavior characterized by a relatively stiff initial elastic response followed by plastic yielding, strain softening and hardening due to chain alignments under large strain. Note that highly nonlinear unloading behavior is then observed, which results in a significant amount of energy dissipation as well as residual strain. The soft TangoPlus material displays hyperelastic rubbery behavior with negligible energy dissipation and hysteresis under cyclic loading conditions. In contrast, the digital materials, where the two base materials were mixed, were found to exhibit significant elastic and inelastic anisotropy during loading and unloading, as evidenced in Figures 1a3 and 1a4. Both the DM1 and DM2 materials printed along the x -direction show greater elastic stiffness than those printed along the y - and z -directions. Beyond the initial elastic regime, pronounced stress-rollover (or yield) and significantly lower flow stress levels are observed in both the DM1 and DM2 materials printed along the x - and y -directions. The unloading behavior of these digital materials is also shown to be strongly orientation-dependent. Specifically, upon unloading, the energy dissipation and residual strain were found to be greater when printing was conducted along the z -direction. The stress-strain curves of the digital materials printed along the z - and x -directions are further reduced to the ratios of the elastic stiffnesses, energy dissipation levels and residual strains as a function of the volume fraction of TangoPlus, as plotted in Figures 1b1 and 1b2. Given that the densities of VeroBlackPlus ($1.17 \sim 1.18 \text{ g/cm}^3$) and TangoPlus ($1.12 \sim 1.13 \text{ g/cm}^3$) are nearly identical (Stratasys 2025a; Stratasys 2025b), the es-

timated material consumption during the printing process of digital materials was directly used to determine the volume fractions of TangoPlus and VeroBlackPlus in these materials (e.g., Slesarenko and Rudykh 2018). As shown in Figure 1b1, both the DM2 ($E_z/E_x \sim 0.6$) and DM1 ($E_z/E_x \sim 0.7$) materials exhibit very strong (initial) elastic anisotropy, while the base materials (VeroBlackPlus and TangoPlus) are elastically isotropic ($E_z/E_x \sim 1.0$). The DM2 material also shows pronounced orientation dependence in both the energy dissipation and residual strain ($D_z/D_x \sim 2.5$ and $R_z/R_x \sim 4.9$), as presented in Figure 1b2, while the DM1 material shows moderate inelastic anisotropy ($D_z/D_x \sim 1.6$ and $R_z/R_x \sim 2.1$). In contrast, the base materials were found to exhibit nearly isotropic mechanical resilience and energy dissipation ($D_z/D_x \sim 1.0$ and $R_z/R_x \sim 1.0$). These experimental results clearly show that mechanical anisotropy emerges in these multi-material, 3D-printed digital materials. More importantly, these digital materials exhibit markedly different mechanical anisotropy at small vs. large strains (see Figures 1a3 and 1a4); the digital materials printed along the deposition direction (z-direction) were found to exhibit lower initial elastic stiffness yet substantially higher flow stresses at increasing strains, accompanied by greater energy dissipation and residual strain upon unloading compared to those printed along the x- and y-directions; i.e., $E_x > E_z$ ($E_y \sim E_z$) at small strain while $D_x < D_z$ ($D_y < D_z$) and $R_x < R_z$ ($R_y < R_z$) under large strain, as clearly highlighted in Figures 1b1 and 1b2.

3 Microscopy characterization of microstructures

We then examined the microstructural features underlying the digital materials (DM1 and DM2) using a high-resolution optical microscope (HRX-01, HiRox). To this end, each digital material specimen was mounted in a hard acrylic resin using a cylindrical mold and subsequently polished (MECATECH 250 SPI, Presi) with abrasive papers of progressively finer grit sizes; initial grinding was performed with 120-grit paper, followed by polishing with 400-, 800-, 1200-, 2400-, and 4000-grit papers to obtain an optically smooth surface suitable for an optical microscopy analysis. Figure 2 presents representative optical microscopy images of the cross-sections on the zx- and xy-planes of the DM1 and DM2 materials. The relatively hard and soft domains in these digital materials (mixtures of VeroBlackPlus and TangoPlus) appear as the dark and bright regions in the images, respectively. Due to the higher volume fraction of VeroBlackPlus, the dark regions in the DM1 materials appear broader than those in the

DM2 materials. Importantly, as shown in Figures 2a1 and 2b1, the zx -plane cross-sectional images reveal well-aligned elliptical hard domains with high aspect ratios embedded within the surrounding soft matrix, in good agreement with optical microscopy images reported in previous studies (Mueller et al. 2017; Zorzetto et al. 2020). The length of the major axis of the elliptical hard domains was found to be approximately 130 - 160 μm , as depicted in Figure 2a2, which is greater than the nominal resolution of the 3D printer in the x -direction ($\sim 40 \mu\text{m}$; Stratasys 2018). These microstructural features are mainly attributed to the combined effects of diffusion between the two photocurable base resins (VeroBlackPlus and TangoPlus), as well as roller leveling in each layer during the multi-material jetting process (Mueller et al. 2017; Zorzetto et al. 2020). Given that these base resins share constituent monomers, they readily mix and diffuse into one another (Mueller et al. 2017; Lei et al. 2018). Moreover, the length of the minor axis was found to be close to 16 μm , nearly identical to the nominal resolution in the z -direction (Stratasys 2018), as shown in Figures 2a2 and 2b2. This is mainly due to the layer-by-layer curing process as the printing progresses, during which the base resins are deposited onto a previously photocured layer, resulting in negligible diffusion and mixing across the printed layers (Lei et al. 2018; Zorzetto et al. 2020; De Noni et al. 2022). It should also be noted that due to the

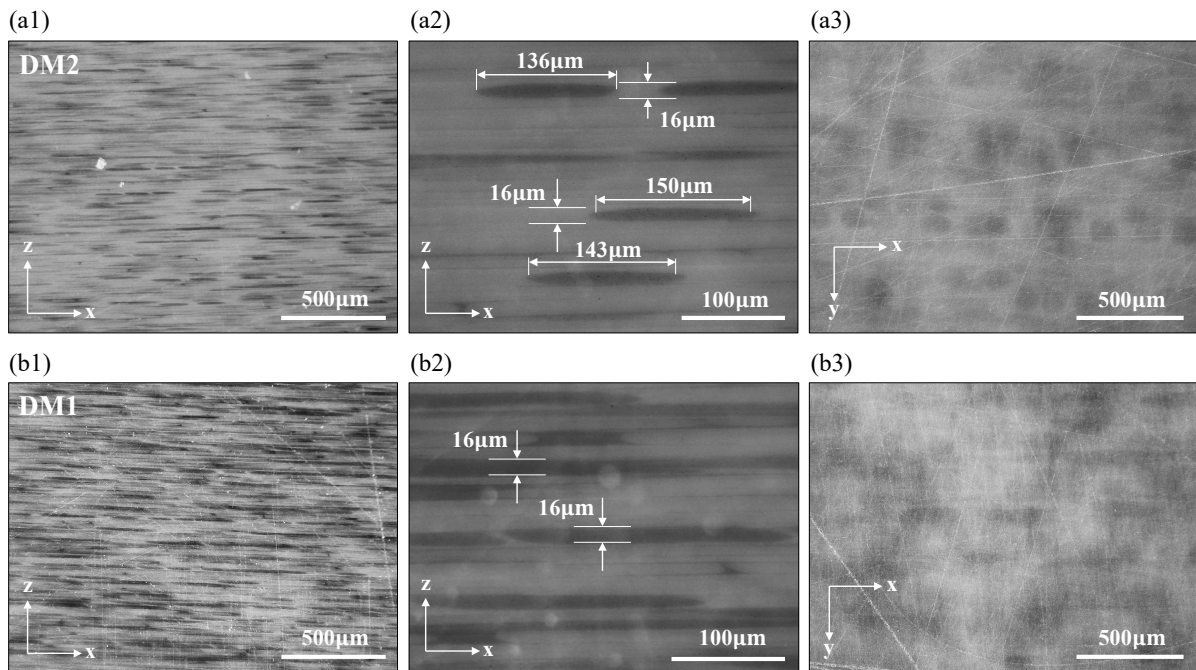


Figure 2: Microstructures of representative 3D-printed digital materials. Optical microscopy images of zx -plane cross-sections and the corresponding magnified views for (a1) and (a2) DM2 and (b1) and (b2) DM1 materials. (a3) and (b3) show the optical microscopy images of xy -plane cross-sections for the DM2 and DM1 materials, respectively.

high volume fraction of VeroBlackPlus ($\sim 36\%$), elliptical hard domains overlap significantly in the zx -plane of the DM1 materials, as shown in Figure 2b2. Furthermore, hard domains with elliptical cross-sections of moderate aspect ratios are observed in the xy -plane images of the digital materials, as shown in Figures 2a3 and 2b3. However, clearly distinguishing the hard domains from the surrounding soft matrix was difficult due to the high optical transparency of the TangoPlus material as well as the small thickness of each printed layer. As an alternative, we fabricated specimens consisting of an array of VeroBlackPlus pillars (elongated along the z -direction) embedded in a TangoPlus matrix, as displayed in Figure A.1 in Appendix A. Each VeroBlackPlus pillar was set to have a square cross-section of $40\ \mu\text{m} \times 40\ \mu\text{m}$ on the xy -plane, corresponding to the nominal resolution of the 3D printer in the x - and y -directions. However, as shown in Figure A.1d in Appendix A, the elliptical cross-sections of the VeroBlackPlus pillars were found to have average major and minor axis lengths of approximately $152\ \mu\text{m}$ ($\pm 36\ \mu\text{m}$) and $95\ \mu\text{m}$ ($\pm 25\ \mu\text{m}$), respectively. This observation further supports that significant diffusion and mixing between the photocurable base resins occurs within each layer during the multi-material printing process. Microscopy characterization of the 3D-printed digital materials reveals the key microstructural features essential for constructing a representative volume element for micromechanical analysis. In particular, the orientation-dependent diffusion and mixing between the photocurable base resins leads to the formation of strongly anisotropic microstructures comprising two distinct domains.

4 Micromechanical analysis

4.1 Construction of representative volume elements

Next, we present a simple procedure for designing a representative volume element (RVE) that captures the key microstructural features of the digital materials. We note that the RVEs are mainly taken to be two-dimensional for the micromechanical analysis; i.e., we construct RVEs that mimic the microstructures observed in the zx -cross-sections of the digital materials (e.g., see Figure 2). The micromechanical modeling results for these two-dimensional RVEs are then presented together with experimental data for plane-strain compression of the digital materials in Figures 4, 5 and 6. Furthermore, under uniaxial compressive loading conditions, we examine the printing-orientation-dependent mechanical behavior by constructing three-dimensional RVEs, especially for the DM2 materials in Figure 7.

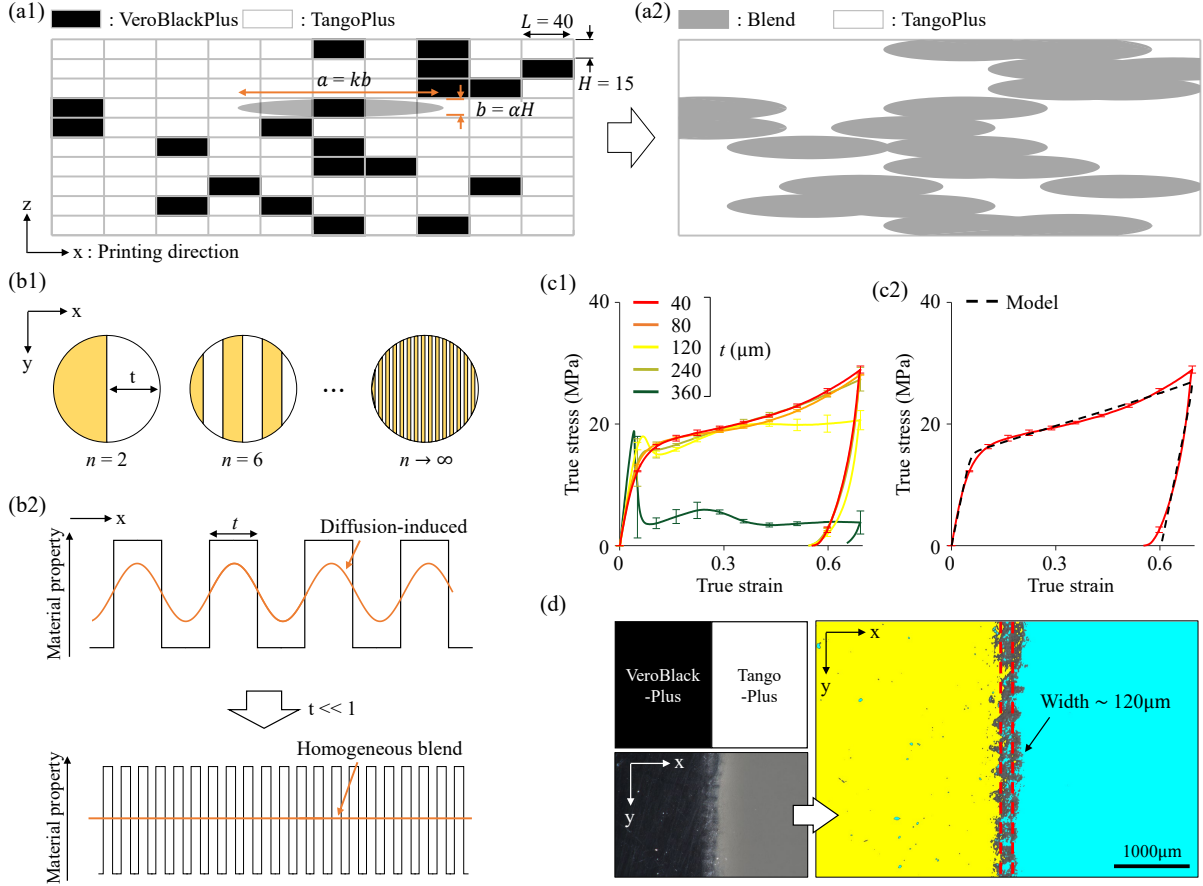


Figure 3: Construction of representative volume elements (RVEs) for 3D-printed digital materials. (a1) Schematic of the deposition pattern of the photocurable base resins (VeroBlackPlus and TangoPlus) on the zx -plane together with (a2) the corresponding RVE comprising well-aligned, high-aspect-ratio elliptical hard domains embedded within the surrounding soft matrix. (b1) Schematic illustration of cylindrical specimens comprising n alternating VeroBlackPlus/TangoPlus layers along the x -direction with a layer thickness t ; (b2) as the number of VeroBlackPlus/TangoPlus layers (n) increases (or the layer thickness t decreases), a macroscopic response close to that of the homogeneous blend can be obtained due to diffusion and mixing between the photocurable base resins. (c1) Stress-strain curves at a strain rate of 0.01 s^{-1} for the cylindrical specimens with varying layer thicknesses ($t = 40, 80, 120, 240$ and $360 \text{ }\mu\text{m}$). (c2) Comparison of the macroscopic stress-strain responses measured experimentally (solid line) and predicted numerically (dashed line) for cylindrical specimens with $t = 40 \text{ }\mu\text{m}$. (d) A broad, blurred interfacial region across VeroBlackPlus and TangoPlus layers along the x -direction.

Figure 3a1 schematically presents the deposition pattern of the two base resins on the zx -plane; note that the unit cells corresponding to the deposition locations of VeroBlackPlus and TangoPlus resins are displayed in black and white, respectively. Here, the length, L , and the height, H , of each cell are taken to be the nominal resolutions of the 3D-printer along the x - ($\sim 40\mu\text{m}$) and z - ($\sim 15\mu\text{m}$) directions. In each layer, VeroBlackPlus cells are randomly selected based on the volume fraction of VeroBlackPlus (v_{VB}), as estimated from the consumption of

the VeroBlackPlus material during the printing process of the digital materials. For example, as shown in Figure 3a1, two VeroBlackPlus cells out of ten cells are selected when constructing the RVEs for the DM2 materials with $v_{\text{VB}} \sim 20\%$. Then, to account for diffusion and mixing between the photocurable base resins, the selected VeroBlackPlus cells are replaced by ellipses placed at their centers, as schematically illustrated in Figures 3a1 and 3a2. The minor axis length of the ellipse, b , is defined as $b = \alpha H$, where α is introduced to account for interlayer diffusion and mixing. The major axis length of the ellipse, a , is then defined as $a = kb$, where k is the aspect ratio due to both diffusion and roller leveling within each layer. We further note that the elliptical “hard” domains are modeled as a homogeneous 50%/50% blend of VeroBlackPlus and TangoPlus while the remaining “soft” domains are taken to be pure TangoPlus; i.e., all VeroBlackPlus resins are assumed to diffuse and be mixed with the TangoPlus resins of equal mass in each case. Under this assumption, the total mass fraction of the elliptical hard domains is twice the estimated VeroBlackPlus consumption during the printing process of the digital materials. By also assuming that the densities of the two base materials and their blends are nearly identical, the corresponding “effective” volume fraction of the elliptical hard domains is taken to be $v_{\text{hard}} = 2v_{\text{VB}}$ ¹. In other words, these elliptical hard domains are assumed not only to exhibit a softer response than the hard base material (VeroBlackPlus) but also to occupy a larger volume fraction effectively within each of the RVEs. Using v_{hard} , the pairs of k and α for the elliptical hard domains are then simply determined. To characterize the “effective” stress-strain responses of this homogeneous blend (i.e., mixed VeroBlackPlus and TangoPlus domains in gray in Figure 3a2), we fabricated cylindrical specimens comprising n alternating VeroBlackPlus/TangoPlus layers along the x-direction, each with a thickness of t , as depicted in Figure 3b1. Here, it was further assumed that when the number of layers (n) becomes sufficiently large, a macroscopic response close to that of the homogeneous blend or mixed domain can be obtained due to diffusion and mixing between the photocurable base resins, as schematically illustrated in Figure 3b2. Mechanical tests of these specimens with varying layer thicknesses ($t = 40, 80, 120, 240$ and $360 \mu\text{m}$) were then conducted under uniaxial compression along the deposition direction (z-direction) at a strain rate of 0.01 s^{-1} . As displayed in Figure 3c1, when $t \geq 120 \mu\text{m}$, the specimens exhibit stress-strain responses that significantly vary with the layer thickness, indicating that homogeneous mixing of the base resins was not achieved in these

¹Note that the densities of VeroBlackPlus and TangoPlus are $1.17 \sim 1.18 \text{ g/cm}^3$ and $1.12 \sim 1.13 \text{ g/cm}^3$, respectively.

specimens at this point. In particular, for the specimens with $t = 360 \mu\text{m}$, thin and discrete VeroBlackPlus layers are formed between the interfacial regions where diffusion and mixing occurs. Consequently, these specimens with $t = 360 \mu\text{m}$ show much greater elastic stiffness, followed by a sudden stress drop due to the structural collapse of these thin VeroBlackPlus layers under compression. In contrast, the stress-strain responses of the specimens with $t = 40 \mu\text{m}$ and $80 \mu\text{m}$ are nearly identical at small to large strain levels. These results suggest that these layers ($t < 80 \mu\text{m}$) are sufficiently thin to yield a homogeneous blend through diffusion and mixing between the base resins. The corresponding model prediction of the stress-strain behavior of this blend is shown along with the representative experimental data (for $t = 40 \mu\text{m}$) in Figure 3c2; see Appendix B for detailed information of the finite deformation constitutive models for the homogeneous blend and pure TangoPlus. This approach for estimating the effective constitutive behavior of the hard domains is further supported by the optical microscopy images of a specimen comprising two alternating VeroBlackPlus/TangoPlus layers along the x-direction shown in the left insets of Figure 3d. A broad, blurred interfacial region is observed on the xy-plane images of the specimen, as shown in the right inset of Figure 3d. Because the alternating VeroBlackPlus and TangoPlus layers are stacked along the printing direction, the boundaries of the interfacial region appear wavy rather than straight, consistent with optical microscopy images reported in previous studies (Liu et al. 2020). Importantly, the width of the interfacial region ($\sim 120 \mu\text{m}$) is much greater than the layer thicknesses of the specimens, which exhibit nearly identical stress-strain responses ($t = 40 \mu\text{m}$ and $80 \mu\text{m}$), further supporting that the large-strain mechanical behavior of these specimens can be used to model the elliptical hard domains in RVEs.

4.2 Experiments vs. micromechanical models

Figure 4 presents the micromechanical modeling results of the RVEs along with the experimental data for the DM1 materials. Here, α was set to 1.0, 1.2, 1.4 and 1.6, representing the degree of interlayer diffusion and mixing. For each α , the corresponding aspect ratio k due to the combined effects of diffusion between the TangoPlus and VeroBlackPlus resins and roller leveling in each layer was determined such that v_{hard} across five statistical realizations of the RVEs was approximately 72% (note that $v_{\text{VB}} \sim 36\%$ for the DM1 materials). Consequently, as depicted in Figure 4a, the RVEs comprising the elliptical hard domains with $k = 9.3, 6.7, 5.0$ and 3.9 were obtained. As k increases (or with a decrease of α), the connectivity of these hard domains

increases in the x-direction but decreases in the z-direction. Also, due to the high v_{hard} in these digital materials, the well-aligned elliptical domains are more likely to overlap along the x-direction, particularly in the RVEs with $k = 9.3$ and $\alpha = 1.0$, as observed in the microscopy images of the DM1 materials on the zx-plane (see Figure 2). A micromechanical analysis of these RVEs was then conducted under macroscopic plane-strain compression along the z- and x-directions. Boundary value problems of the RVEs were solved using Abaqus/Standard. The

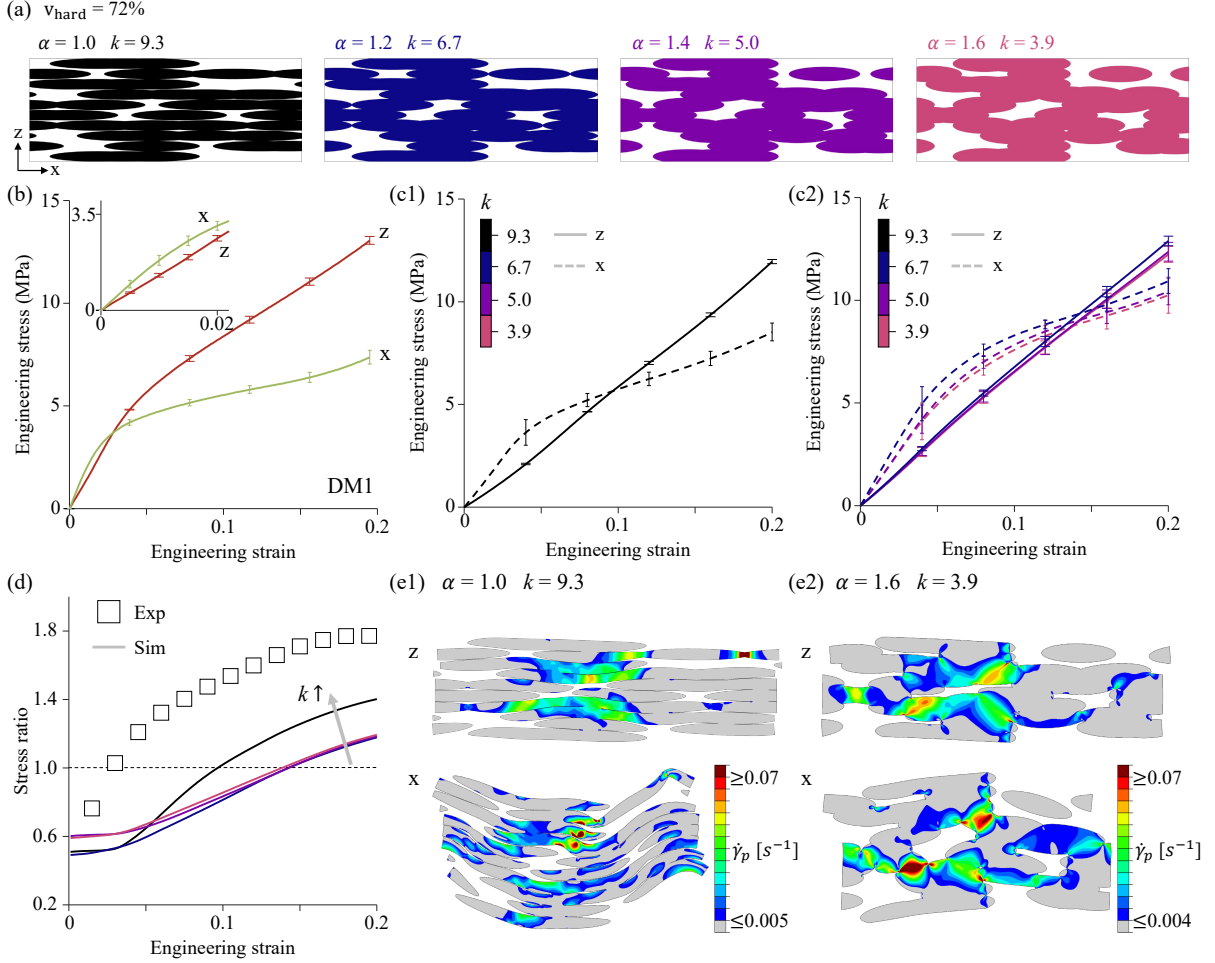


Figure 4: Experiments vs. micromechanical modeling results for the DM1 materials. (a) Representative volume elements for the DM1 materials ($v_{\text{hard}} \sim 72\%$) comprising elliptical hard domains with $k = 9.3, 6.7, 5.0$ and 3.9 . (b) Stress-strain curves (experiments) of the DM1 materials subjected to plane-strain compression along the global z- and x-axes at a strain rate of 0.01 s^{-1} . Orientation-dependent mechanical behavior of RVEs (numerical simulations) with (c1) $k = 9.3$ and (c2) $k = 6.7, 5.0$ and 3.9 . (d) Stress ratios, defined as the stress along the z-direction relative to that along the x-direction in experiments (open symbols) and numerical simulations (solid lines). Contours of the plastic shear strain rate $\dot{\gamma}_p$ in the deformed configurations of hard domains within RVEs with (e1) $k = 9.3$ and (e2) $k = 3.9$ loaded in the z- (upper insets) and x-directions (lower insets) at a macroscopic strain level of 0.15 ; here, only elliptical hard domains are displayed.

macroscopic average responses of the RVEs were computed under periodic boundary conditions using the fictitious node virtual work method. Additionally, we used four-node bilinear elements with reduced integration and hourglass control (CPE4R). Furthermore, in order to examine the predictive capability of the proposed two-dimensional micromechanical models, plane-strain compression tests of the 3D-printed digital materials were additionally conducted at a strain rate of 0.01 s^{-1} . To this end, specimens were placed in a fixture that restricts deformation in the out-of-plane direction (y -direction) and were subjected to compressive loading along the global z - or x -axes; we also followed the standard experimental protocols that have been widely used to characterize the large deformation behavior of polymeric materials under plane-strain conditions (Arruda and Boyce 1993). As plotted in Figure 4b, the stress-strain responses of the DM1 materials were found to be highly orientation-dependent at small to large strains, very similar to those observed under uniaxial compression (see Figure 1a3). It should be noted that the digital materials loaded in the x -direction exhibit higher initial elastic stiffness ($E_x > E_z$) yet substantially lower flow stress levels when under large strains than in the z -direction. Interestingly, the micromechanical modeling results of the RVEs with the highest aspect ratio ($k = 9.3$ and $\alpha = 1.0$) nicely capture the key features of the experimentally measured stress-strain curves of the DM1 materials at small to large strain levels, as shown in Figure 4c1. It is also important to note that the aspect ratios of the well-aligned elliptical hard domains observed in the optical microscopy images were found to be approximately 8 - 10 (see Figure 2). The RVEs with smaller aspect ratios (i.e., $k = 6.7, 5.0$ and 3.9) exhibit more gradual stress-rollover that occurs at considerably higher strain levels than with $k = 9.3$ when loaded in the x -direction, as shown in Figure 4c2. These stress-strain curves with varying aspect ratios in the elliptical hard inclusions are reduced further to normalized stress, defined as the stress along the z -direction relative to that along the x -direction. As plotted in Figure 4d, under small strains (< 0.03), the stress ratios remain below 1.0 due to the greater “initial” elastic stiffness when loaded in the x -direction. The stress ratios increase near the strain levels at which stress-rollover occurs in this loading direction. In particular, due to the pronounced rollover in the stress-strain curves of the RVEs with the highest aspect ratio, $k = 9.3$, the stress ratio in these RVEs exhibits a dramatic upturn followed by a substantial increase under large strains, which is also clearly observed in the experimental data for the DM1 materials.

The anisotropic responses of the digital materials are also assessed by examining how the RVEs deform under the two loading directions. Figures 4e1 and 4e2 present the contours of the

plastic shear strain rates $\dot{\gamma}_p$ of two exemplar RVEs with high and low aspect ratios ($k = 9.3$ and 3.9) under macroscopic imposed strain of 0.15 ; the von Mises stress contours $\bar{\sigma}$ in these RVEs at a macroscopic strain level of 0.01 is presented in Figures C.4a1 and C.4a2 in Appendix C. At small strains, much greater stress develops throughout the elliptical hard domains when these domains are aligned with the loading direction (i.e., when loaded in the x-direction); the effects of well-aligned elliptical (or ellipsoidal) inclusions on elastic anisotropy have been widely reported in many classes of heterogeneous materials (Sheng et al. 2004; Saadat et al. 2015; Raney et al. 2018; Mo et al. 2020). However, as the macroscopic strain increases, the RVEs become mechanically unstable when loaded in the aligned direction of the high-aspect-ratio inclusions, as numerically predicted in the lower insets of Figures 4e1 and 4e2. More importantly, the RVEs with the highest aspect ratio ($k = 9.3$) were found to undergo severe instability accompanied by local buckling of the elliptical hard domains (the lower inset of Figure 4e1). These micromechanical modeling results reveal that the apparent stress-rollover observed in the RVEs with $k = 9.3$ loaded in the x-direction result from local buckling and severe plastic deformation of these hard domains. It should be noted that even with no significant local buckling, relatively gradual stress-rollover is observed in the RVEs with the lowest aspect ratio ($k = 3.9$) loaded in the x-direction; see the stress-strain curve (the pink dashed line) in Figure 4c2 and the lower inset of Figure 4e2. This is primarily attributed not only to plastic deformation in the elliptical hard domains aligned well with the loading direction but to finite rotation of these domains in the soft matrices. Either local buckling or finite rotation of the elliptical hard domains in the RVEs loaded in the x-direction occurs because these deformation modes are energetically more favorable than the uniform compression of the hard domains under large deformation (Moraleta et al. 2009; Gutttag and Boyce 2015; Avazmohammadi and Castaneda 2016; Zhao et al. 2016; Slesarenko and Rudykh 2017). In contrast, when loaded in the z-direction, both RVEs with $k = 9.3$ and 3.9 deform with no instability, as displayed in the upper insets of Figures 4e1 and 4e2. Moreover, because the elliptical hard inclusions are perpendicular to the loading direction, they experience less significant plastic deformation, resulting in negligible stress-rollover and much higher stress responses at large strain levels, as shown in the simulated stress-strain curves (solid lines) in Figures 4c1 and 4c2. These results indicate that while the initial elastic anisotropy in the 3D-printed digital materials primarily results from stable compressive deformation of the high-aspect-ratio elliptical inclusions highly interconnected along the aligned direction, anisotropy under large strain is governed by local buckling as well as plastic deformation of these hard

domains.

The micromechanical modeling results are also presented in Figure 5 of the RVEs of the DM2 materials. Here, v_{hard} across five statistical realizations was set to approximately 40%. RVEs with varying aspect ratios ($k = 8.0, 5.5, 4.1$ and 3.2) were then constructed with the same set of α used for the RVEs of the DM1 materials (i.e., $\alpha = 1.0, 1.2, 1.4$ and 1.6), as displayed in Figure 5a. Due to the relatively low v_{hard} , the elliptical hard domains are less connected

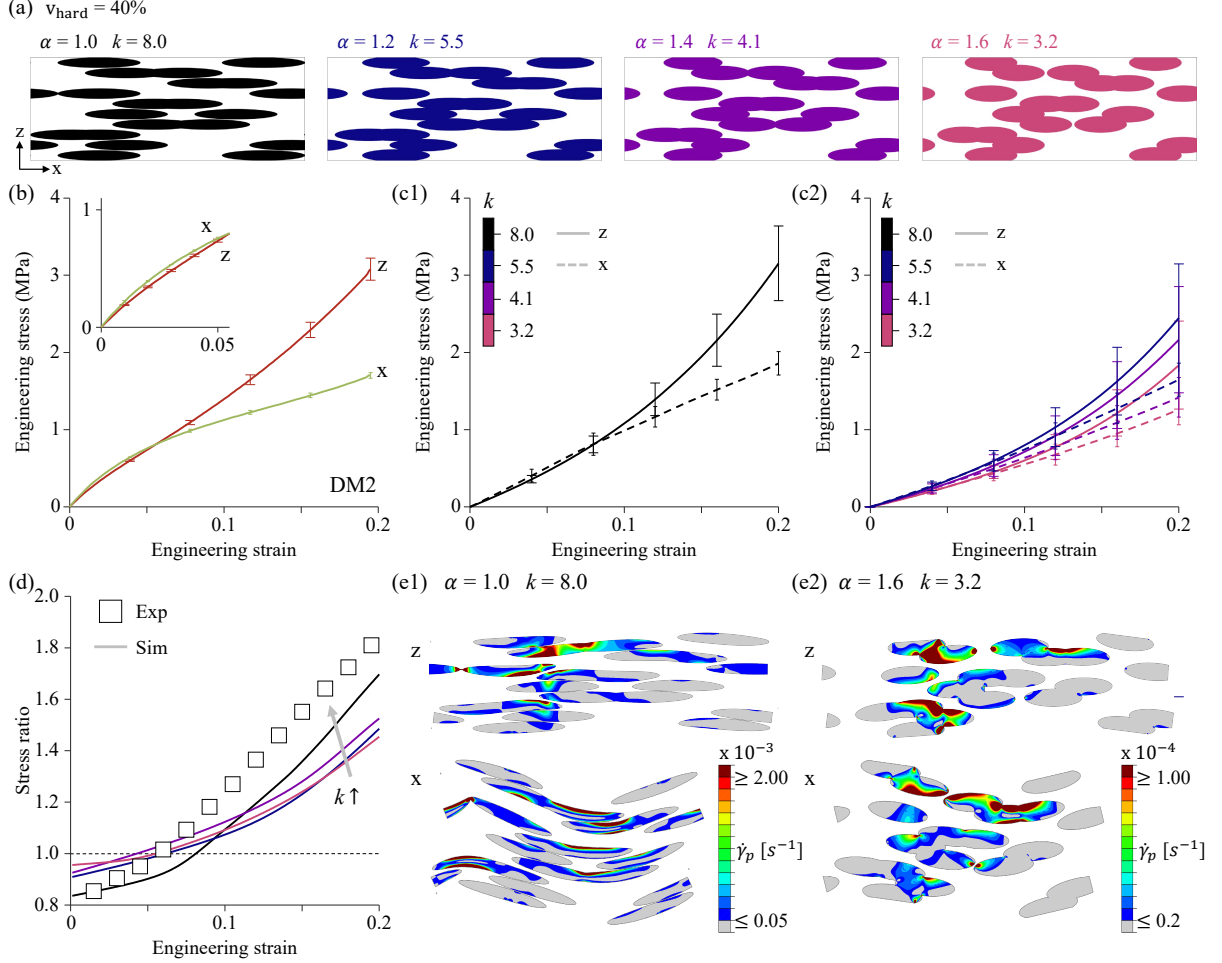


Figure 5: Experiments vs. micromechanical modeling results for the DM2 materials. (a) Representative volume elements for the DM2 materials ($v_{\text{hard}} \sim 40\%$) comprising elliptical hard domains with $k = 8.0, 5.5, 4.1$ and 3.2 . (b) Stress-strain curves (experiments) of the DM2 materials subjected to plane-strain compression along the global z - and x -axes at a strain rate of 0.01 s^{-1} . Orientation-dependent mechanical behavior of RVEs (numerical simulations) with (c1) $k = 8.0$ and (c2) $k = 5.5, 4.1$ and 3.2 . (d) Stress ratios, defined as the stress along the z -direction relative to that along the x -direction in experiments (open symbols) and numerical simulations (solid lines). Contours of the plastic shear strain rate $\dot{\gamma}_p$ in the deformed configurations of hard domains within RVEs with (e1) $k = 8.0$ and (e2) $k = 3.2$ loaded in the z - (upper insets) and x -directions (lower insets) at a macroscopic strain level of 0.15 ; here, only elliptical hard domains are displayed.

(or overlapped) than in the RVEs for the DM1 materials. Figures 5b, 5c1 and 5c2 present the macroscopic stress-strain responses of the DM2 materials in experiments and numerical simulations. The RVEs with the highest aspect ratio ($k = 8.0$ and $\alpha = 1.0$) best match the experimental data. More specifically, when loaded in the x-direction, these RVEs exhibit greater initial elastic stiffness yet substantially lower flow stress levels under increasing strains. This is further supported by the stress ratio (the stress in the z-direction relative to that in the x-direction) which exceeds 1.0 with an increase in the macroscopic strain, after which it increases substantially under large strains, as plotted in Figure 5d. The mechanical anisotropy in these RVEs was found to decrease significantly with smaller aspect ratios ($k = 5.5, 4.1$ and 3.2) from small to large strain levels. The numerically predicted stress-strain responses are examined further through the plastic shear strain rate and von Mises stress contours in the deformed configurations of two exemplar RVEs with $k = 8.0$ and 3.2 . At the early stage of loading, the alignment of the elliptical hard domains along the loading direction gives rise to greater elastic stiffness, especially in the RVEs with the highest aspect ratio ($k = 8.0$), as clearly evidenced by the von Mises stress contours shown in Figures C.4b1 and C.4b2 in Appendix C. Beyond the initial elastic regime, buckling instabilities were found to emerge in the RVEs with $k = 8.0$. However, the elliptical hard inclusions with $k = 3.2$ exhibit finite rotation rather than local buckling, as shown in the lower insets of Figures 5e1 and 5e2. Furthermore, as shown in the upper insets of Figures 4e1 and 4e2, both RVEs with $k = 8.0$ and $k = 3.2$ deform without any instability when loaded in the z-direction. Interestingly, the stress ratio in the DM2 materials continues to increase significantly under large strains ($> \sim 0.15$), as evidenced in both the experiments and the numerical simulations (with $k = 8.0$, solid black line), as presented in Figure 5d. However, the stress ratio in the DM1 materials (Figure 4d) was found not to increase yet to level off under large strain levels. This is primarily attributed to the large volume fraction of the hyperelastic soft matrices in the DM2 materials ($v_{\text{soft}} \sim 60\%$). When loaded especially in the z-direction, the DM2 materials undergo negligible plastic deformation but exhibit rubbery features characterized by a pronounced stress upturn due to chain orientation or locking at large strain levels; as shown in the upper insets of Figures 5e1 and 5e2, plastic flows with much smaller magnitudes develop throughout the elliptical hard inclusions compared to those in the DM1 materials with $v_{\text{hard}} \sim 72\%$ (Figures 4e1 and 4e2). The comparisons of the experiments and numerical simulations presented in Figures 4 and 5 further demonstrate that the highly orientation-dependent mechanical behavior of these digital materials (DM1 and DM2) is nicely

captured in the RVEs with $\alpha = 1.0$. The micromechanical modeling results were also found to be very consistent with what we observed through the optical microscopy analysis, which revealed that interlayer diffusion and mixing is significantly suppressed, compared to intralayer diffusion and mixing between the photocurable base resins (VeroBlackPlus and TangoPlus) in each layer (e.g., see Figure 2). More importantly, the intralayer diffusion and mixing resulted in higher connectivity between the hard elliptical inclusions along the printing direction (i.e., x-direction), by which these “connected” hard domains have much higher “effective” aspect ratios. Therefore, when loaded along the alignment direction, local buckling of these high-aspect-ratio hard inclusions becomes energetically more favorable than finite rotation, leading to the more pronounced stress-rollover observed in both the DM1 and DM2 materials. We note that buckling instabilities have also been experimentally observed in 3D-printed composites, where a soft base resin (TangoPlus) is used for the surrounding matrix and either a hard base resin (VeroBlackPlus) or digital materials (DM1 and DM2) is used for the high-aspect-ratio hard inclusions (Li et al. 2013; Slesarenko and Rudykh 2016; Li et al. 2018; Arora et al. 2022; Kaynia et al. 2025).

5 Discussion and further implications

Numerous micromechanical modeling strategies have been proposed to predict the effective elastic properties of additively manufactured materials with significant microstructural heterogeneities (Mo et al. 2020; Nawafleh and Celik 2020; Groetsch et al. 2023), including digital materials (Meisel et al. 2018; De Noni et al. 2022). Those micromechanical approaches have yet to fully capture the complex deformation mechanisms underlying the large strain mechanical behavior strongly dependent on the printing orientation. In this work, we have presented a methodology that combines large strain mechanical testing, microscopy characterization and micromechanical modeling to explore the mechanical anisotropy observed in 3D-printed digital materials at small to large strains. Representative volume elements have been proposed to mimic realistic anisotropic microstructures resulting from orientation-dependent diffusion and mixing between photocurable base resins during the printing process. The micromechanical modeling results of the RVEs presented in Figures 4 and 5 clearly show that the high-aspect-ratio elliptical hard domains play a central role in the emergence of mechanical anisotropy in the digital materials from small to large strains. Stable compressive deformation of the high-aspect-ratio

elliptical inclusions interconnected along the printing direction was found to give rise to the “initial” elastic anisotropy, with $E_x/E_z \sim 1.21$ and 1.16 correspondingly for the representative DM1 and DM2 materials assessed experimentally along with $E_x/E_z \sim 1.90$ and 1.18 in the micromechanical modeling results of RVEs with $k = 9.3$ and $k = 8.0$, respectively. The interplay between local buckling and plastic deformation of the hard domains has been found to govern the mechanical anisotropy, especially under large strains.

• Resilience and dissipation of the digital materials upon unloading

These digital materials also exhibit strongly orientation-dependent mechanical resilience and energy dissipation upon unloading, as demonstrated by plane-strain tests of the DM1 materials under loading and unloading conditions (Figure 6a). When loaded in the z-direction, greater energy dissipation ($D_z/D_x \sim 1.3$) and residual strain ($R_z/R_x \sim 1.9$) were observed. However, as shown in Figure 6b, the RVEs with $k = 9.3$ and $\alpha = 1.0$ loaded in the x-direction (dashed gray line) were found to exhibit greater energy dissipation and greater residual strain than those loaded in the z-direction (solid gray line; $D_z/D_x \sim 0.87$ and $R_z/R_x \sim 0.94$). The digital materials here were simply modeled as two-phase composites with a very large stiffness ratio between the hard and soft components ($\mu_{\text{hard}}/\mu_{\text{soft}}$), which resulted in a discrepancy between the experimental data and model predictions. It should also be noted that in the micromechanical analysis presented in Figures 4 and 5, the stiffness ratio was approximately 400. In many previous studies of two-phase materials comprising hard inclusions embedded within surrounding soft matrices, such large stiffness ratios have been shown to degrade significantly the energy dissipation and load transfer capabilities through the hard inclusions (Sheng et al. 2004; Lee et al. 2024a; Cho et al. 2024); i.e., most of the imposed macroscopic deformation is accommodated through surrounding matrices which are much softer than the inclusions. This is further supported by the contours of the plastic strain rates in the RVEs of the DM1 materials under macroscopic strain of 0.2. As shown in the upper inset of Figure 6c1, when loaded in the z-direction, significant plastic flows do not develop throughout the elliptical hard domains because the imposed macroscopic deformation is largely accommodated by the hyperelastic soft domains. Importantly, when loaded in the x-direction, the elliptical hard domains exhibit significant deformation through buckling, as shown in the lower inset of Figure 6c1. Consequently,

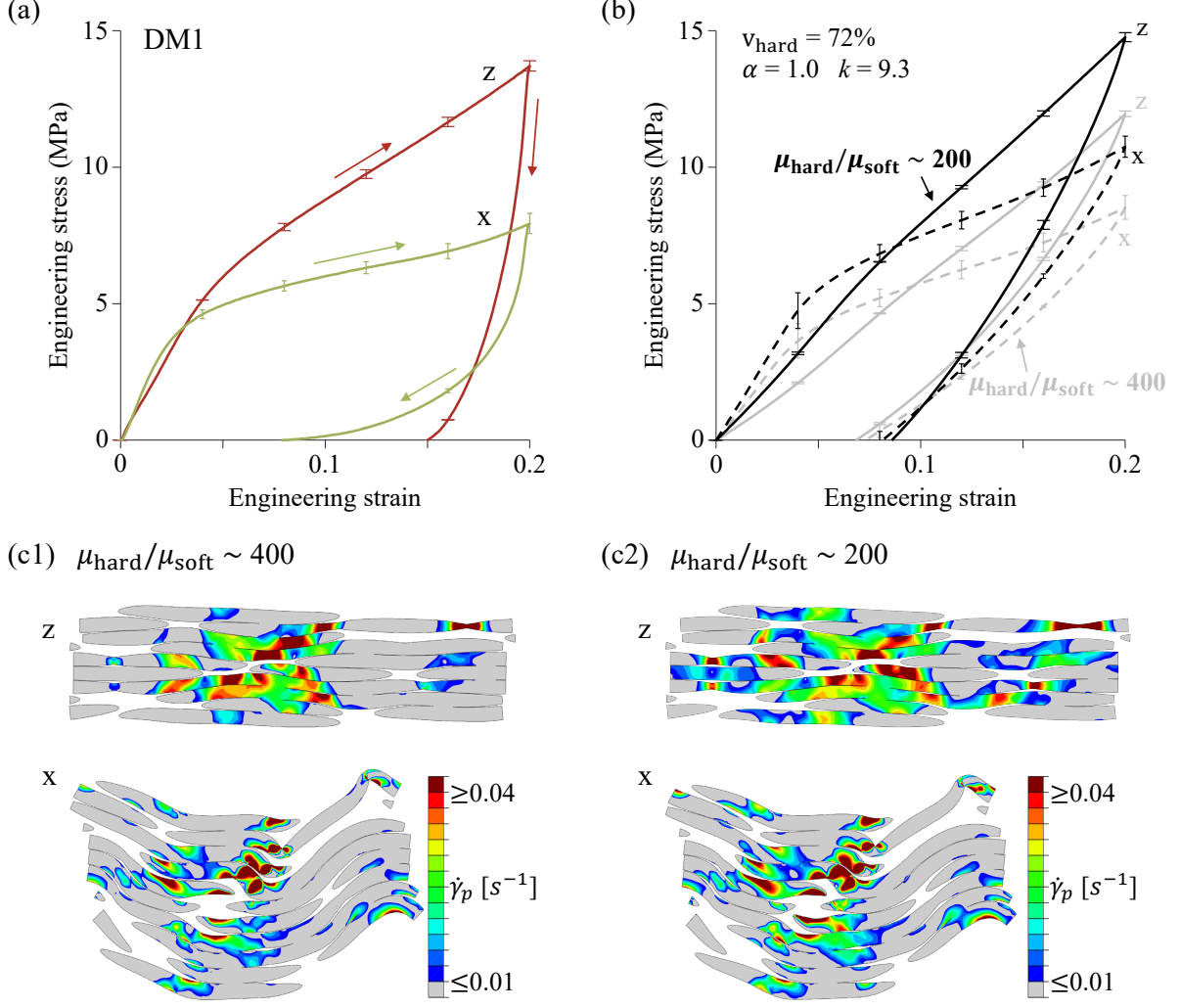


Figure 6: Printing-orientation-dependent mechanical resilience and energy dissipation of 3D-printed digital materials. (a) Stress-strain curves (experiments) of the DM1 materials loaded in the z- and x-directions under plane-strain conditions at a strain rate of 0.01 s^{-1} . (b) Orientation-dependent mechanical behavior of RVEs (numerical simulations) for the DM1 materials ($k = 9.3$ and $\alpha = 1.0$) with $\mu_{\text{hard}}/\mu_{\text{soft}} \sim 400$ (gray lines) and $\mu_{\text{hard}}/\mu_{\text{soft}} \sim 200$ (black lines) loaded in the z- (solid lines) and x-directions (dashed lines). Contours of the plastic shear strain rate $\dot{\gamma}_p$ in the deformed configurations of hard domains in RVEs with (c1) $\mu_{\text{hard}}/\mu_{\text{soft}} \sim 400$ and (c2) $\mu_{\text{hard}}/\mu_{\text{soft}} \sim 200$ loaded in the z- (upper insets) and x-directions (lower insets) at a macroscopic strain level of 0.2; here, only elliptical hard domains are displayed.

strong plastic flows also develop throughout the buckled regions of these hard domains. Furthermore, when the RVEs deform with no instability at small strain, the elliptical inclusions aligned along the loading direction undergo more pronounced plastic deformation. Combined, these all contribute to the large amount of energy dissipation in the RVEs loaded in the x direction, resulting in $D_x > D_z$ in our micromechanical analysis. For further examination of the effect of the stiffness ratio on the printing-orientation-dependent energy dissipation capability,

we conducted additional micromechanical analysis of the RVEs with $k = 9.3$ and $\alpha = 1.0$ by simply varying the elastic modulus of the soft component from $\mu_{\text{soft}} = 0.26$ MPa to 0.52 MPa (i.e., $\mu_{\text{hard}}/\mu_{\text{soft}} \sim 200$). As plotted in Figure 6b, both energy dissipation and residual strain were found to increase with the decreased stiffness ratio (i.e., from $\mu_{\text{hard}}/\mu_{\text{soft}} \sim 400$ to 200). Importantly, these RVEs with the lower stiffness ratio exhibited greater energy dissipation as well as greater residual strain when loaded in the z-direction; i.e., $D_x < D_z$ and $R_x < R_z$. This is further supported by the plastic strain rate contours in the elliptical hard domains. As shown in the upper inset of Figure 6c2, when loaded in the z-direction, significantly larger regions of the elliptical hard domains undergo plastic deformation, compared to those in the RVEs with $\mu_{\text{hard}}/\mu_{\text{soft}} \sim 400$ (Figure 6c1). In contrast, in the RVEs loaded in the x-direction, plastic flows develop primarily within the buckled hard domains under large strain, as shown in the lower inset of Figure 6c2, similar to the RVEs with $\mu_{\text{hard}}/\mu_{\text{soft}} \sim 400$ (Figure 6c1). It should also be noted that when these RVEs deform with no instability at small strain, decreasing the stiffness ratio results in much stronger plastic flows that develop throughout the hard inclusions perpendicular to the loading direction. However, because buckling instabilities occur at very low strain levels (< 0.05), decreasing the stiffness ratio does not significantly influence the energy dissipation and load transfer capabilities in these RVEs loaded in the x-direction. These results also suggest that the interplay between buckling instability and plastic deformation of the well-aligned elliptical hard domains governs not only the mechanical anisotropy under large strain but also the orientation-dependent resilience and energy dissipation capabilities in these 3D-printed digital materials.

- **Micromechanical modeling results of three-dimensional RVEs subjected to uniaxial compression**

We have presented micromechanical analysis of representative digital materials (DM1 and DM2) subjected to plane-strain compression using the two-dimensional RVEs in Figures 4, 5 and 6. We note that relative deformations between the hard and soft domains through the out-of-plane direction (here, y-direction) do not play a crucial role in the overall mechanical features of the DM1 materials, as the volume fraction of the hard domains ($v_{\text{hard}} \sim 72\%$) is relatively high (e.g., Boyce et al. 2001a; Boyce et al. 2001b; Cho et al. 2024). In contrast, for the DM2 materials with $v_{\text{hard}} \sim 40\%$, deformation through the out-of-plane direction may become important, which

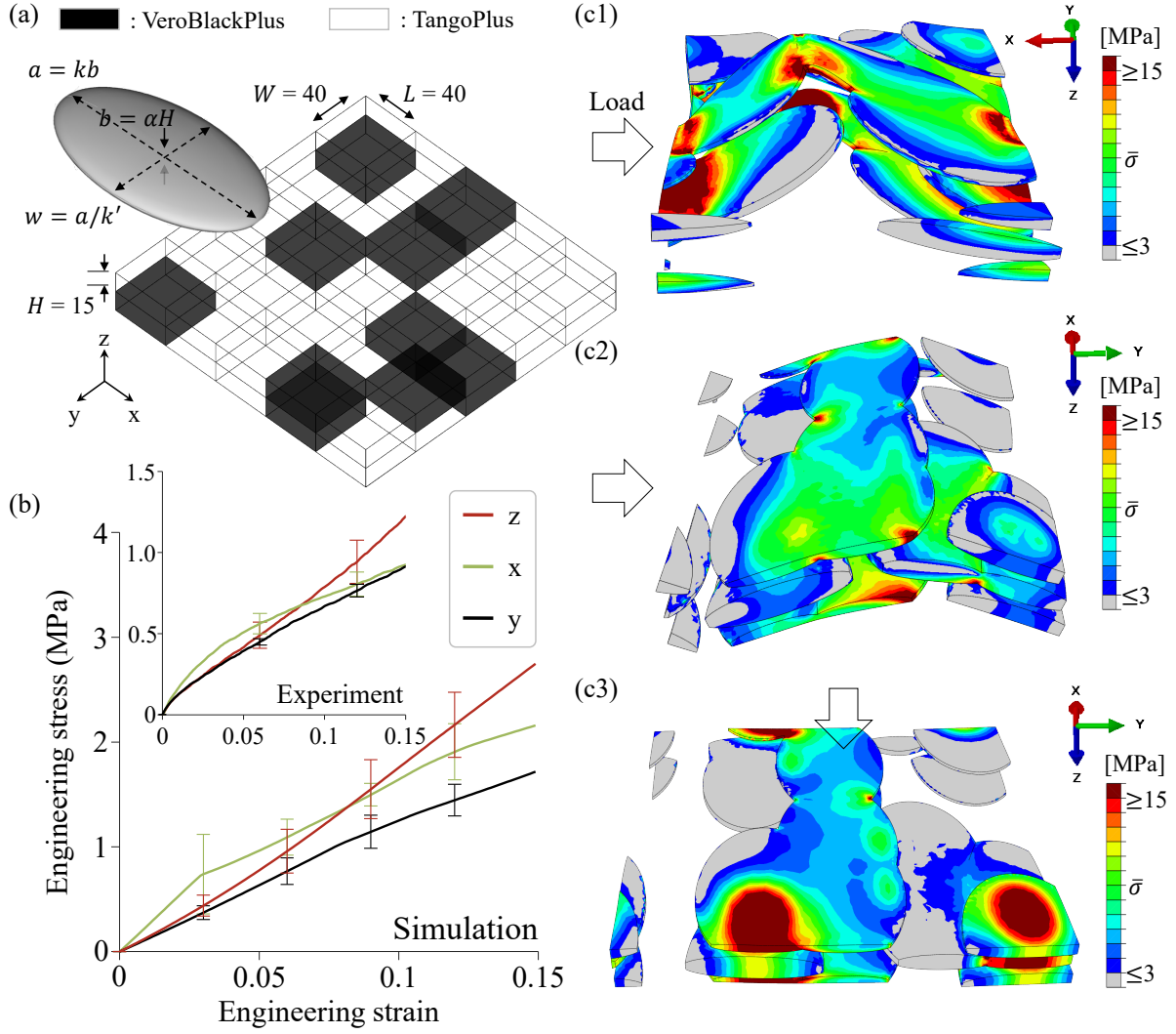


Figure 7: Micromechanical modeling results of three-dimensional representative volume elements (RVEs). (a) Schematic of the three-dimensional deposition pattern of the photocurable base resins (VeroBlackPlus and TangoPlus) together with an ellipsoidal inclusion used to construct hard domains in the three-dimensional setting. (b) Orientation-dependent stress-strain curves of three-dimensional RVEs for the DM2 materials ($v_{\text{hard}} \sim 40\%$) with $k = 7.0$, $k' = 1.6$ and $\alpha = 1.0$ uniaxially compressed in the x-, y- and z-directions (inset: experimental stress-strain curves of the DM2 materials subjected to uniaxial compression along the global x-, y- and z-axes at a strain rate of 0.01 s^{-1}). Contours of the von Mises stress ($\bar{\sigma}$) in the deformed configurations of hard domains in RVEs loaded in the (c1) x-, (c2) y- and (c3) z-directions at a macroscopic strain level of 0.15; here, only ellipsoidal hard domains are displayed.

cannot be fully captured through a micromechanical analysis of two-dimensional RVEs. Here, the printing-orientation-dependent mechanical behavior of the DM2 materials is investigated further through a micromechanical analysis of three-dimensional RVEs subjected to uniaxial compression with no lateral geometric constraints; the micromechanical modeling results are compared with the uniaxial experimental data for the DM2 materials presented in Figure 1a4.

As schematically illustrated in Figure 7a, we started with three-dimensional deposition patterns of photocurable base resins (VeroBlackPlus and TangoPlus). Here, the width, W , of each cell is taken to be the nominal resolution of the 3D-printer along the y -direction ($\sim 40 \mu\text{m}$). From the VeroBlackPlus volume fraction in the DM2 materials ($v_{\text{VB}} \sim 20\%$), five VeroBlackPlus cells were randomly selected in each layer of 5 by 5 cells on the xy -plane. These VeroBlackPlus cells were then replaced by ellipsoidal inclusions with dimensions a , w and b along the x -, y - and z -axes, respectively. The ellipsoidal dimension along the z -direction was set to $b = \alpha H$, with $\alpha = 1.0$ to account for the suppressed interlayer diffusion and mixing between the base resins (see Figure 2). The aspect ratio of the elliptical cross-section of the ellipsoidal hard domains on the xy -plane was taken to be $k' = 1.6$ from what we observed in the specimens comprising VeroBlackPlus pillars embedded in a TangoPlus matrix, as shown in Figure A.1 in Appendix A. For $\alpha = 1.0$ and $k' = 1.6$, the aspect ratio of the elliptical cross-section on the zx -plane, k , was determined such that the volume fraction of the ellipsoidal hard domains was $v_{\text{hard}} \sim 40\%$, similarly to the two-dimensional RVE construction presented in Figure 3. We then conducted a micromechanical analysis of the RVEs constructed using three different deposition patterns under uniaxial compression along the x -, y - and z -directions; note that the material parameters used in the micromechanical analysis of two-dimensional RVEs were used here as well to model the hard inclusions and the surrounding soft matrices. Figure 7b presents the macroscopic stress-strain responses of the three-dimensional RVEs for the DM2 materials. For comparison, experimentally measured stress-strain curves of the DM2 materials up to a strain of 0.15 are also displayed in the inset of Figure 7b. In both the experiments and numerical simulations, the DM2 materials show macroscopic responses strongly dependent on the loading direction at small to large strain levels. Importantly, the numerical predictions of these three-dimensional RVEs reproduce the experimental results reasonably well. Under small strain, the RVEs loaded in the x -direction were found to exhibit greater initial elastic stiffness than those in the y - and z -directions ($E_x/E_z \sim 1.8$ and $E_y/E_z \sim 0.9$); i.e., $E_x > E_z$ and $E_y \sim E_z$. Because the well-aligned ellipsoidal hard domains are less connected along the y -direction, the elastic stiffening effect is weaker than that along the x -direction. Beyond the initial elastic regime, the stress-rollover is observed in the RVEs loaded not only in the x -direction but also in the y -direction. In particular, the RVEs loaded in the y -direction are found to exhibit less apparent stress-rollover than those loaded in the x -direction. This is further evidenced by the deformed configurations of these three-dimensional RVEs under macroscopic strain of 0.15. As shown in Figures 7c1 and 7c2, the

RVEs loaded in the x- and y-directions become mechanically unstable with an increase in the macroscopic strain. More importantly, when loaded in the y-direction, the ellipsoidal hard inclusions predominantly undergo finite rotation (see Figure 7c2) due to their lower effective aspect ratios on the yz-plane ($w/b = 4.375$) compared to those on the zx-plane ($a/b = 7.0$). However, as shown in Figure 7c1 for the RVEs loaded in the x-direction, significant local buckling throughout the hard domains leads to more pronounced stress-rollover, similar to the two-dimensional RVEs with $k = 8.0$ (see Figure 5e1). Furthermore, as shown in Figure 7c3, when loaded in the z-direction, highly stable compressive deformation with negligible plastic deformation of the ellipsoidal hard domains results in negligible stress-rollover and much higher stress responses at large strains. The micromechanical modeling results of these three-dimensional RVEs further demonstrate that the two-dimensional approximation used for the DM2 materials with $v_{\text{hard}} \sim 40\%$ presented in Figure 5 is sufficient to capture their microscopic deformation mechanisms; i.e., when loaded in either the x- or z-direction, the overall deformation features are primarily governed by in-plane microstructural mechanisms rather than out-of-plane deformations. These three-dimensional RVEs with multiple ellipsoidal inclusions nicely capture the complex, anisotropic mechanical behavior of the DM2 materials from small to large strains under uniaxial conditions; however, employing RVEs with a larger number of ellipsoidal hard domains remains limited due to the high computational cost.

6 Conclusion

In this work, we have addressed, through a combination of mechanical experiments, microscopy analysis and micromechanical modeling, the deformation mechanisms responsible for the printing-orientation-dependent mechanical behavior of multi-material, 3D-printed digital materials, especially at large strains. Uniaxial and plane-strain compression tests clearly showed that mechanical anisotropy emerges in the 3D-printed digital materials under small to large strain levels. Specifically, these digital materials printed along the deposition direction (z-direction) have been found to exhibit lower initial elastic stiffness yet substantially higher flow stresses at increasing strains, accompanied by greater energy dissipation and residual strain upon unloading than those printed along the printing direction (x-direction). Microscopy characterization of the 3D-printed digital materials further revealed microstructural heterogeneities comprising two distinct hard and soft domains formed by orientation-dependent diffusion and mixing be-

tween photocurable base resins. Through a micromechanical analysis of representative volume elements that account for the key geometric features of the microstructures, we demonstrated that the proposed modeling framework can successfully predict the mechanical anisotropy of digital materials at small to large strains. At the early stage of deformation, stable compression of the high-aspect-ratio elliptical hard domains was shown to be responsible for the greater elastic stiffness in the digital materials when loaded in the printing direction. More importantly, our experimental and micromechanical modeling results showed that buckling instability coupled with plastic deformation of elliptical hard domains highly interconnected along the printing direction governs not only the mechanical anisotropy but the printing-orientation-dependent resilience and energy dissipation capabilities in these digital materials at large strains.

A comprehensive mechanistic understanding of the printing-orientation-dependent damage and fracture behavior of these 3D-printed digital materials remains beyond the scope of this work. More specifically, investigations on the toughening mechanisms in a broad range of 3D-printed digital materials with hard inclusions embedded in the surrounding soft matrices or *vice versa* would be of critical interest in future. Towards this end, a new computational methodology involving the phase-field or gradient-damage approach can be useful as these digital materials undergo large deformation prior to final failure (Talamini et al. 2018; Narayan and Anand 2021; Lee et al. 2023a; Lee et al. 2024b). Further, the micromechanical modeling framework presented here can be extended to account for more realistic chemical compositions of these digital materials. The 3D-printed digital materials studied in this work have been found to have gradual variations in their composition and mechanical properties across the interfaces between hard and soft domains (Mueller et al. 2017; Liu et al. 2020; Zorzetto et al. 2020). These interfacial regions across hard and soft domains, also known as interphases, have been shown to influence not only the nonlinear elastic responses (Qu et al. 2011; Goudarzi et al. 2015) but also the load transfer and energy dissipation capabilities (Ortiz and Boyce 2008; Li et al. 2020). In our work, however, complex microstructural and chemo-mechanical features at the interphases were not considered; instead, sharp, perfectly bonded interfaces were assumed. While the present micromechanical models provide useful mechanistic insights into the mechanical anisotropy of these digital materials, particularly at large strains, they do not account for all major aspects of the experimentally measured responses. A more detailed characterization and modeling of interphases would enable more accurate predictions of the printing-orientation-dependent macroscopic responses of these digital materials. Finally, we note that most previous studies of architected materials (or

mechanical metamaterials) were conducted, assuming that these 3D-printed digital materials are elastically and inelastically isotropic. Through the micromechanical modeling approaches presented in this work, which explicitly capture the printing-orientation-dependent mechanical features, the mechanical performance and functionalities of architected materials can be fully exploited from small to large strains.

Appendix A Further microscopy analysis on hard inclusions in a soft matrix in digital materials

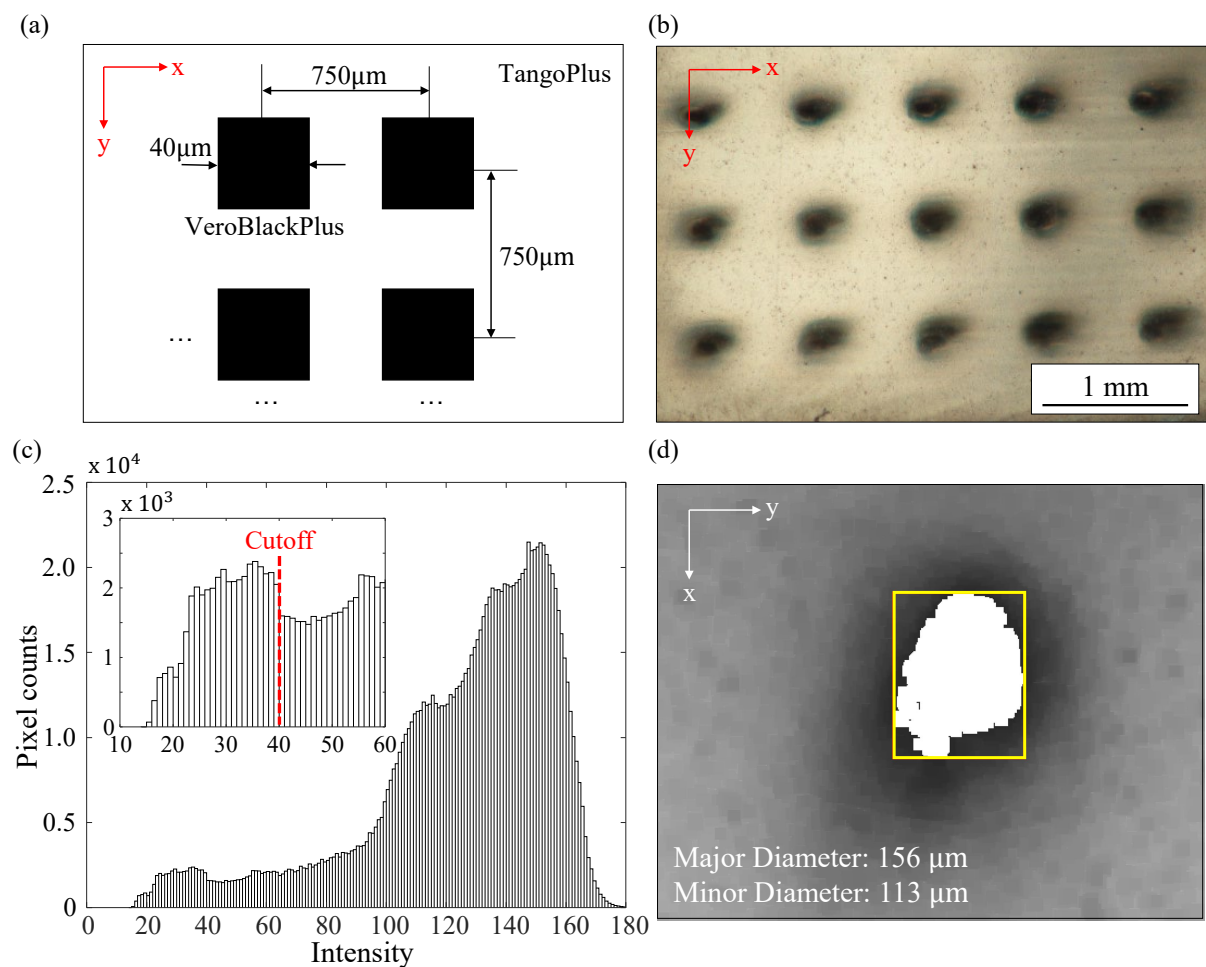


Figure A.1: Orientation-dependent diffusion and mixing between photocurable base resins. (a) Schematic of an array of VeroBlackPlus pillars embedded within a TangoPlus matrix. (b) Optical microscopy image of an xy -plane cross-section of a 3D-printed specimen. (c) Intensity histogram of a representative grayscale image that shows a single hard domain embedded within the surrounding soft matrix (inset: magnified histogram of the low-intensity region together with the cutoff intensity used to distinguish dark and bright regions in the grayscale images). (d) Resulting binarized image of a hard domain with an elliptical cross-section on the xy -plane.

Diffusion and mixing between the two photocurable base resins (VeroBlackPlus and TangoPlus) during the printing processes presented in Figure 2 was further examined by fabricating specimens comprising an array of VeroBlackPlus pillars (elongated along the z-direction) embedded in a TangoPlus matrix, as schematically illustrated in Figure A.1a. A representative optical microscopy image of the xy-plane cross-section of these specimens is shown in Figure A.1b. For better preprocessing the raw optical images, only the red and green channels were used for grayscale conversion as the blue channel exhibited insufficient intensity contrast between the dark and bright regions. Specifically, the xy-plane cross-sections of the VeroBlackPlus pillars (dark regions in Figure A.1b) exhibited peak intensities of 38 - 40 across all RGB channels while the surrounding TangoPlus matrix (bright regions) showed peak intensities of 155 - 165 in the red and green channels but only about 125 in the blue channel. Furthermore, since the top and bottom surfaces of the specimens are not perfectly parallel, the VeroBlackPlus pillars appear slightly tilted with respect to the optical axis of the microscope (i.e., global z-axis). To avoid overestimating the xy-plane cross-sectional areas of the VeroBlackPlus pillars, a cutoff intensity of 40/255 was selected from the grayscale histogram, corresponding to the value at which the pixel count associated with the dark regions decreases sharply, as shown in Figure A.1c. As presented in Figure A.1d, binarization using this intensity threshold yields segmented pillar cross-sections that are well approximated by ellipses, with the average major and minor axis lengths of approximately 152 μm ($\pm 36 \mu\text{m}$) and 95 μm ($\pm 25 \mu\text{m}$), respectively. This additional microscopy analysis further supports our assumption that the elliptical (or ellipsoidal) hard domains exhibit an effectively larger volume fraction than v_{VB} due to diffusion and mixing between photocurable base resins during the printing process.

Appendix B Mechanical behavior of hard and soft components: experiments and constitutive modeling

Figure B.2 presents the stress-strain behavior of the hard (a homogeneous 50%/50% blend of VeroBlackPlus and TangoPlus) and soft (pure TangoPlus) components under uniaxial compression at a strain rate of 0.01 s^{-1} . The hard component exhibits a relatively stiff initial response, followed by yield-like stress rollover and strain hardening. The soft component shows a much more compliant stress-strain response.

We then present finite deformation constitutive modeling framework for the hard and soft

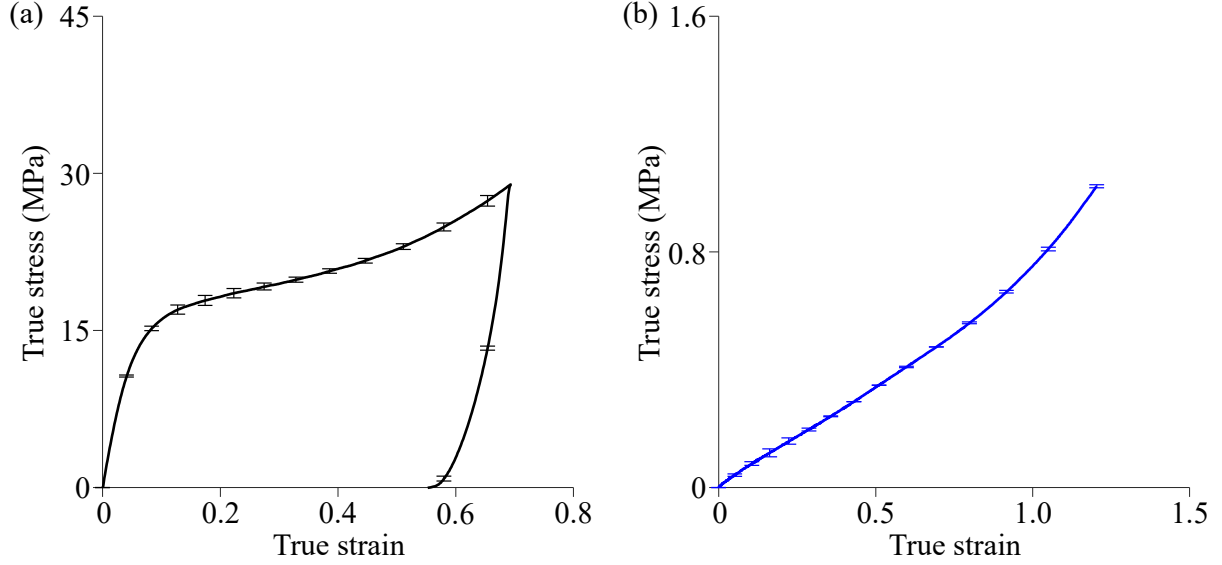


Figure B.2: Stress-strain behavior of (a) the hard component and (b) the soft component under uniaxial compression at a strain rate of 0.01 s^{-1} in experiments.

components employed in the micromechanical analysis. The constitutive model of the hard component comprises (1) a time-dependent elastic-viscoplastic mechanism (denoted I) and (2) a time-independent hyperelastic mechanism (denoted N). We then define the following basic kinematic fields for the hard component:

$$\begin{aligned}
 \mathbf{F} &\stackrel{\text{def}}{=} \frac{\partial \boldsymbol{\varphi}}{\partial \mathbf{X}} = \mathbf{F}_I = \mathbf{F}_N && \text{deformation gradient that maps material points in a reference } (\mathbf{X}) \\
 &&& \text{to points in a deformed configuration } (\mathbf{x} = \boldsymbol{\varphi}(\mathbf{X}, t); \boldsymbol{\varphi}: \text{motion}) \\
 \mathbf{F}_I &= \mathbf{F}_I^e \mathbf{F}_I^p && \text{decomposition of } \mathbf{F}_I \text{ into elastic } (\mathbf{F}_I^e) \text{ and plastic } (\mathbf{F}_I^p) \text{ parts;} \\
 \mathbf{F}_I^e &= \mathbf{R}_I^e \mathbf{U}_I^e && \text{polar decomposition of } \mathbf{F}_I^e \text{ into rotation } (\mathbf{R}_I^e) \text{ and stretch } (\mathbf{U}_I^e); \\
 \bar{\mathbf{F}}_N &= J^{-1/3} \mathbf{F}_N && \text{isochoric part of } \mathbf{F}_N; \\
 \bar{\mathbf{B}}_N &= \bar{\mathbf{F}}_N \bar{\mathbf{F}}_N^\top && \text{isochoric left Cauchy-Green tensor.}
 \end{aligned}$$

The deformation rate is described by the velocity gradient $\mathbf{L} \stackrel{\text{def}}{=} \text{grad} \mathbf{v}$ which is decomposed into elastic (\mathbf{L}_I^e) and plastic (\mathbf{L}_I^p) parts,

$$\begin{aligned}
 \mathbf{L} &= \dot{\mathbf{F}} \mathbf{F}^{-1} \\
 &= \dot{\mathbf{F}}_I^e \mathbf{F}_I^{e-1} + \mathbf{F}_I^e \dot{\mathbf{F}}_I^p \mathbf{F}_I^{p-1} \mathbf{F}_I^{e-1} \\
 &= \mathbf{L}_I^e + \mathbf{F}_I^e \mathbf{L}_I^p \mathbf{F}_I^{e-1}.
 \end{aligned} \tag{B.1}$$

The plastic part of the velocity gradient is $\mathbf{L}_I^p = \mathbf{D}_I^p + \mathbf{W}_I^p$, where \mathbf{D}_I^p is the rate of plastic

stretching and \mathbf{W}_I^p is the plastic spin. Furthermore, we make two important kinematical assumptions for plastic flow; the flow is incompressible (i.e., $\det \mathbf{F}_I^p = 1$) and irrotational (i.e., $\mathbf{W}_I^p = 0$). Thus, the rate of change in the plastic deformation gradient is given by,

$$\dot{\mathbf{F}}_I^p = \mathbf{D}_I^p \mathbf{F}_I^p. \quad (\text{B.2})$$

The Cauchy stress (\mathbf{T}_I) in the time-dependent elastic-viscoplastic mechanism I is expressed by,

$$\mathbf{T}_I = \frac{1}{J} \mathbf{R}_I^e \mathbf{M}_I^e \mathbf{R}_I^{e\top}, \quad (\text{B.3})$$

with the Mandel stress $\mathbf{M}_I^e = 2\mu_I(\ln \mathbf{U}_I^e)_0 + K(\ln J)\mathbf{I}$, the elastic shear modulus μ_I and the bulk modulus K . We note that the total bulk response is lumped into the time-dependent mechanism I. The rate of plastic stretching \mathbf{D}_I^p is assumed to be coaxial to the deviatoric part of the Mandel stress (i.e., $(\mathbf{M}_I^e)_0 = \mathbf{M}_I^e - \frac{1}{3}\text{tr}(\mathbf{M}_I^e)\mathbf{I}$),

$$\mathbf{D}_I^p = \frac{\dot{\gamma}_I^p}{\sqrt{2}} \mathbf{N}_I^p, \quad \text{where} \quad \mathbf{N}_I^p = \frac{(\mathbf{M}_I^e)_0}{\|(\mathbf{M}_I^e)_0\|} \quad \text{and} \quad \|(\mathbf{M}_I^e)_0\| = \sqrt{(\mathbf{M}_I^e)_0 : (\mathbf{M}_I^e)_0}. \quad (\text{B.4})$$

Then, we employ the thermally-activated viscoplasticity model prescribed by,

$$\dot{\gamma}_I^p = \dot{\gamma}_{I,0} \exp \left[-\frac{\Delta G}{k_B \theta} \left\{ 1 - \frac{\bar{\tau}}{s_0} \right\} \right], \quad \text{where} \quad \bar{\tau} = \frac{1}{\sqrt{2}} \|(\mathbf{M}_I^e)_0\|, \quad (\text{B.5})$$

with the reference plastic strain rate $\dot{\gamma}_{I,0}$, the activation energy ΔG , Boltzmann's constant k_B , the absolute temperature $\theta = 295\text{K}$ (room temperature), the shear strength s_0 and the magnitude of the deviatoric part of the Mandel stress $\bar{\tau}$ (i.e., von Mises equivalent shear stress).

The (deviatoric) Cauchy stress (\mathbf{T}_N) in the time-independent hyperelastic mechanism N is given by,

$$\mathbf{T}_N = \frac{\mu_N \lambda_N}{3J \bar{\lambda}} \mathcal{L}^{-1} \left(\frac{\bar{\lambda}}{\lambda_N} \right) (\bar{\mathbf{B}}_N)_0 \quad \text{where} \quad \bar{\lambda} = \sqrt{\frac{\text{tr} \bar{\mathbf{B}}_N}{3}} \quad \text{and} \quad (\bar{\mathbf{B}}_N)_0 = \bar{\mathbf{B}}_N - \frac{1}{3} \text{tr}(\bar{\mathbf{B}}_N) \mathbf{I}, \quad (\text{B.6})$$

with the elastic shear modulus μ_N and the limiting chain extensibility λ_N ; \mathcal{L}^{-1} is the inverse Langevin function with $\mathcal{L}(x) = \coth(x) - \frac{1}{x}$.

Hard component: Time-dependent elastic-viscoplastic mechanism I		
$\mathbf{T}_I = \frac{1}{J} \mathbf{R}_I^e \mathbf{M}_I^e \mathbf{R}_I^{e\top}$, where $\mathbf{M}_I^e = 2\mu_I(\ln \mathbf{U}_I^e)_0 + K(\ln J)\mathbf{I}$	μ_I [MPa]	90.6
	K [GPa]	1.17
$\dot{\gamma}_I^p = \dot{\gamma}_{I,0} \exp\left[-\frac{\Delta G}{k_B\theta} \left\{1 - \frac{\bar{\tau}}{s_0}\right\}\right]$, where $\bar{\tau} = \frac{1}{\sqrt{2}}\ (\mathbf{M}_I^e)_0\ $	ΔG [10^{-20} J]	3.5
	$\dot{\gamma}_{I,0}$ [s^{-1}]	0.04
s_0 [MPa]		9.04
Hard component: Time-independent hyperelastic mechanism N		
$\mathbf{T}_N = \frac{\mu_N \lambda_N}{3J \bar{\lambda}} \mathcal{L}^{-1}\left(\frac{\bar{\lambda}}{\lambda_N}\right) (\bar{\mathbf{B}}_N)_0$	μ_N [MPa]	5.4
	λ_N	$\sqrt{6}$
Soft component		
$\mathbf{T}_{\text{Soft}} = \frac{\mu_S \lambda_S}{3J \bar{\lambda}} \mathcal{L}^{-1}\left(\frac{\bar{\lambda}}{\lambda_S}\right) (\bar{\mathbf{B}})_0 + K_S(J-1)\mathbf{I}$	μ_S [MPa]	0.235
	K_S [MPa]	16.71
	λ_S	$\sqrt{6.5}$

Table B.1: Material parameters used in the constitutive models for hard and soft components.

The total stress in the hard component is then obtained by,

$$\mathbf{T}_{\text{hard}} = \mathbf{T}_I + \mathbf{T}_N. \quad (\text{B.7})$$

A nearly incompressible Arruda-Boyce model is used for the soft component. The Cauchy stress in the soft component is expressed by,

$$\mathbf{T}_{\text{Soft}} = \frac{\mu_S \lambda_S}{3J \bar{\lambda}} \mathcal{L}^{-1}\left(\frac{\bar{\lambda}}{\lambda_S}\right) (\bar{\mathbf{B}})_0 + K_S(J-1)\mathbf{I} \quad \text{where} \quad \bar{\lambda} = \sqrt{\frac{\text{tr}(\bar{\mathbf{B}})}{3}}, \quad (\text{B.8})$$

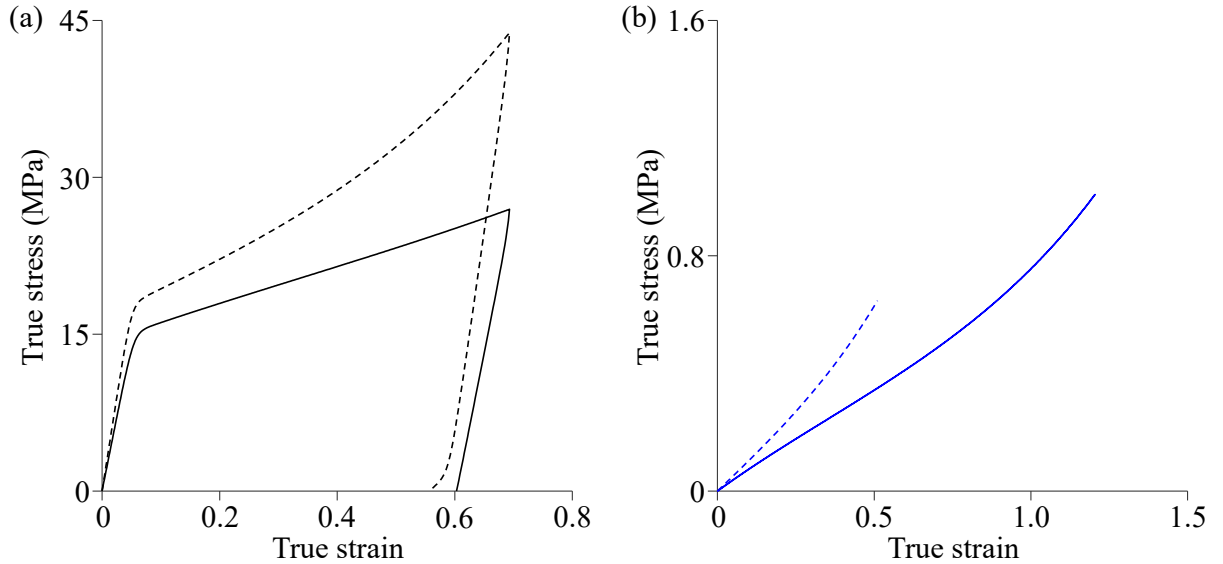


Figure B.3: Stress-strain behavior of (a) the hard component (black lines) and (b) the soft component (blue lines) under uniaxial (solid lines) and plane-strain (dashed lines) compression at a strain rate of 0.01 s^{-1} in numerical simulations.

where μ_S is the elastic shear modulus, K_S is the bulk modulus, λ_S is the limiting chain extensibility, $\bar{\mathbf{B}} = J^{-2/3}\mathbf{F}\mathbf{F}^\top$, \mathbf{F} is the deformation gradient and $\bar{\mathbf{B}}_0$ is the deviatoric part of the isochoric left Cauchy-Green tensor (i.e., $\bar{\mathbf{B}}_0 = \bar{\mathbf{B}} - \frac{1}{3}\text{tr}(\bar{\mathbf{B}})\mathbf{I}$) in the soft component.

Figure B.3 presents the stress-strain curves numerically simulated using the constitutive models for both hard and soft components under uniaxial (solid lines) and plane-strain (dashed lines) compression conditions. The material parameters used in the constitutive models are given in Table B.1.

Appendix C Further micromechanical modeling results

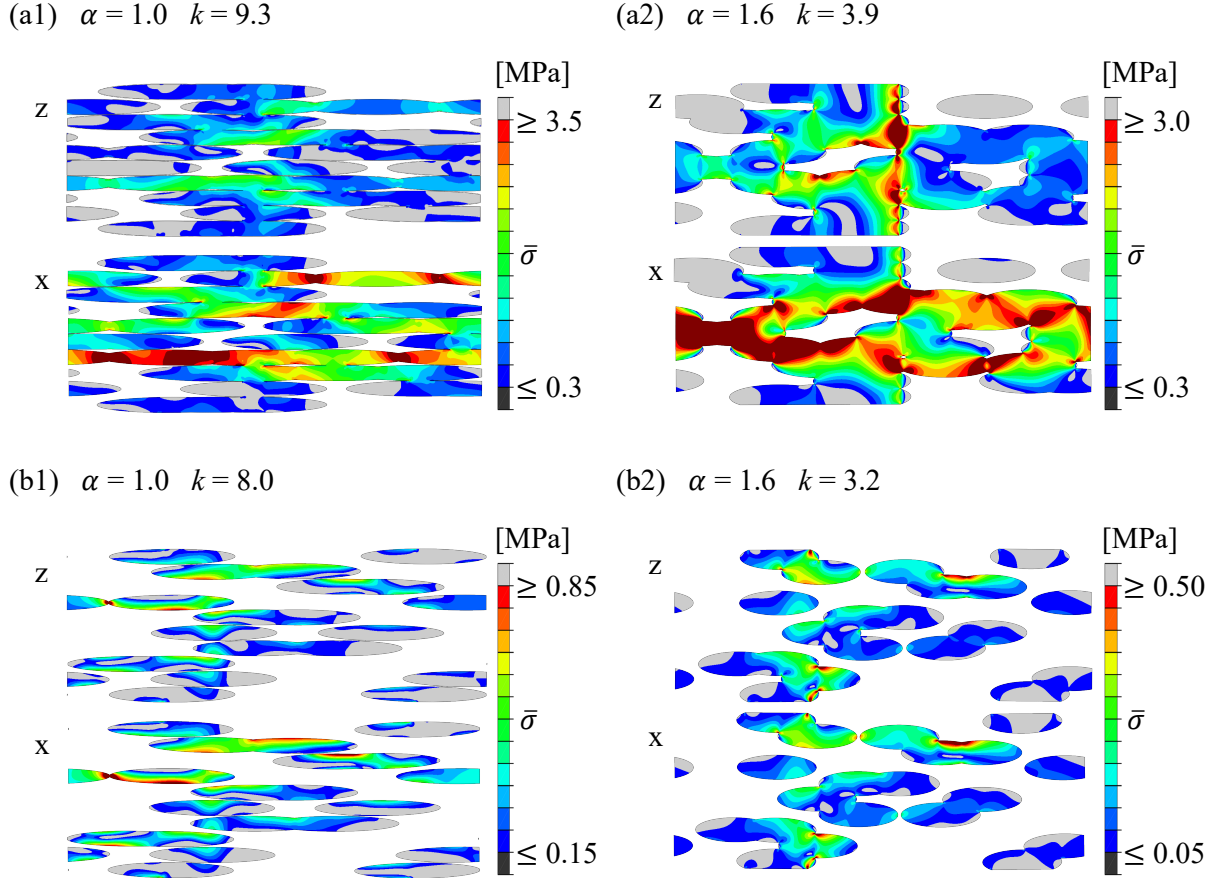


Figure C.4: Contours of the von Mises stress ($\bar{\sigma}$) in the deformed configurations of hard domains in RVEs for the (a1) and (a2) DM1 and (b1) and (b2) DM2 materials loaded in the z- (upper insets) and x-directions (lower insets) at a macroscopic strain level of 0.01; here, only ellipsoidal hard domains are displayed.

We here present the von Mises stress contours in the elliptical hard domains in the RVEs for the DM1 materials with $k = 9.3$ (Figure C.4a1) and 3.9 (Figure C.4a2) at a macroscopic strain

level of 0.01; and the RVEs for the DM2 materials with $k = 8.0$ (Figure C.4b1) and 3.2 (Figure C.4b2). At these early stages of loading, all of the RVEs were found to deform without any instability. Importantly, much greater stress develops throughout the elliptical hard domains in the RVEs loaded along the alignment direction of these domains (x-direction) than those loaded in the z-direction. The von Mises stress contours further demonstrate that the influence of the well-aligned elliptical domains on “initial” elastic anisotropy becomes more pronounced in the RVEs with the highest aspect ratios; i.e., $k = 9.3$ and 8.0 for the DM1 and DM2 materials, respectively.

Acknowledgement

This work was supported by the National Research Foundation of Korea (RS-2023-00279843) and Korea Advanced Institute of Science and Technology (N11250018, N11250083).

References

- Abu-Qbeith, Suhub, Olga Petrenko, Michele Ciavarella, and Stephan Rudykh (2025). “Experimental testing of V notched radially graded materials under static loading”. *Mechanics of Materials*, p. 105364.
- Akbari, Saeed, Amir Hosein Sakhaei, Sahil Panjwani, Kavin Kowsari, Ahmad Serjouei, and Qi Ge (2019). “Multi-material 3D printed soft actuators powered by shape memory alloy wires”. *Sensors and Actuators A: Physical* 290, pp. 177–189.
- Arora, Nitesh, Jian Li, and Stephan Rudykh (2022). “Tunable buckling configurations via in-plane periodicity in soft 3D-fiber composites: Simulations and experiments”. *International Journal of Solids and Structures* 250, p. 111711.
- Arruda, Ellen M and Mary C Boyce (1993). “Evolution of plastic anisotropy in amorphous polymers during finite straining”. *International Journal of Plasticity* 9.6, pp. 697–720.
- Avazmohammadi, Reza and Pedro Ponte Castaneda (2016). “Macroscopic constitutive relations for elastomers reinforced with short aligned fibers: Instabilities and post-bifurcation response”. *Journal of the Mechanics and Physics of Solids* 97, pp. 37–67.
- Bartlett, Nicholas W, Michael T Tolley, Johannes TB Overvelde, James C Weaver, Bobak Mosadegh, Katia Bertoldi, George M Whitesides, and Robert J Wood (2015). “A 3D-printed, functionally graded soft robot powered by combustion”. *Science* 349.6244, pp. 161–165.
- Bass, Lindsey, Nicholas Alexander Meisel, and Christopher B Williams (2016). “Exploring variability of orientation and aging effects in material properties of multi-material jetting parts”. *Rapid Prototyping Journal* 22.5, pp. 826–834.
- Boyce, Mary C, Simona Socrate, Kenneth Kear, Oscar Yeh, and Karla Shaw (2001a). “Micromechanisms of deformation and recovery in thermoplastic vulcanizates”. *Journal of the Mechanics and Physics of Solids* 49.6, pp. 1323–1342.
- Boyce, Mary C, Oscar Yeh, Simona Socrate, Kenneth Kear, and Karla Shaw (2001b). “Micromechanics of cyclic softening in thermoplastic vulcanizates”. *Journal of the Mechanics and Physics of Solids* 49.6, pp. 1343–1360.
- Brown, Nathan C, Daniel C Ames, and Jochen Mueller (2025). “Multimaterial extrusion 3D printing printheads”. *Nature Reviews Materials*, pp. 1–19.
- Buchner, Thomas JK et al. (2023). “Vision-controlled jetting for composite systems and robots”. *Nature* 623.7987, pp. 522–530.
- Cho, Hansohl, Susan Bartyczak, Willis Mock Jr, and Mary C Boyce (2013a). “Dissipation and resilience of elastomeric segmented copolymers under extreme strain rates”. *Polymer* 54.21, pp. 5952–5964.
- Cho, Hansohl, Jaehee Lee, Jehoon Moon, Elmar Pösel, Gregory C Rutledge, Mary C Boyce, et al. (2024). “Large strain micromechanics of thermoplastic elastomers with random microstructures”. *Journal of the Mechanics and Physics of Solids* 187, p. 105615.
- Cho, Hansohl, Steffen Mayer, Elmar Pösel, Markus Susoff, Pieter J in’t Veld, Gregory C Rutledge, and Mary C Boyce (2017). “Deformation mechanisms of thermoplastic elastomers: Stress-strain behavior and constitutive modeling”. *Polymer* 128, pp. 87–99.

- Cho, Hansohl, Renaud G Rinaldi, and Mary C Boyce (2013b). “Constitutive modeling of the rate-dependent resilient and dissipative large deformation behavior of a segmented copolymer polyurea”. *Soft Matter* 9.27, pp. 6319–6330.
- Cho, Hansohl, James C Weaver, Elmar Pösel, Pieter J in’t Veld, Mary C Boyce, and Gregory C Rutledge (2016). “Engineering the mechanics of heterogeneous soft crystals”. *Advanced Functional Materials* 26.38, pp. 6938–6949.
- De Noni, Lorenzo, Laura Zorzetto, Francesco Briatico-Vangosa, Marta Rink, Davide Ruffoni, and Luca Andena (2022). “Modelling the interphase of 3D printed photo-cured polymers”. *Composites Part B: Engineering* 234, p. 109737.
- DebRoy, Tarasankar et al. (2018). “Additive manufacturing of metallic components—process, structure and properties”. *Progress in materials science* 92, pp. 112–224.
- Deschanel, S, BP Greviskes, Katia Bertoldi, SS Sarva, Wei Chen, SL Samuels, RE Cohen, and MC Boyce (2009). “Rate dependent finite deformation stress–strain behavior of an ethylene methacrylic acid copolymer and an ethylene methacrylic acid butyl acrylate copolymer”. *Polymer* 50.1, pp. 227–235.
- Fernandes, Matheus C, Joanna Aizenberg, James C Weaver, and Katia Bertoldi (2021). “Mechanically robust lattices inspired by deep-sea glass sponges”. *Nature Materials* 20.2, pp. 237–241.
- Gibson, Ian, David Rosen, Brent Stucker, Mahyar Khorasani, David Rosen, Brent Stucker, and Mahyar Khorasani (2021). *Additive manufacturing technologies*. Vol. 17. Springer.
- Goudarzi, Taha, Daniel W Spring, Glaucio H Paulino, and Oscar Lopez-Pamies (2015). “Filled elastomers: A theory of filler reinforcement based on hydrodynamic and interphasial effects”. *Journal of the Mechanics and Physics of Solids* 80, pp. 37–67.
- Groetsch, Alexander et al. (2023). “Microscale 3D printing and tuning of cellulose nanocrystals reinforced polymer nanocomposites”. *Small* 19.3, p. 2202470.
- Gu, Dongdong, Xinyu Shi, Reinhart Poprawe, David L Bourell, Rossitza Setchi, and Jihong Zhu (2021). “Material-structure-performance integrated laser-metal additive manufacturing”. *Science* 372.6545, eabg1487.
- Gutttag, Mark and Mary C Boyce (2015). “Locally and dynamically controllable surface topography through the use of particle-enhanced soft composites”. *Advanced Functional Materials* 25.24, pp. 3641–3647.
- Ituarte, Inigo Flores, Narasimha Boddeti, Vahid Hassani, Martin L Dunn, and David W Rosen (2019). “Design and additive manufacture of functionally graded structures based on digital materials”. *Additive Manufacturing* 30, p. 100839.
- Kaynia, Narges, Nicholas Xuanlai Fang, and Mary C Boyce (2025). “Soft-Layered Composites with Wrinkling-Activated Multi-Linear Elastic Behavior, Stress Mitigation, and Enhanced Strain Energy Storage”. *Advanced Engineering Materials* 27.22, p. 2400750.
- Klein, Dominik K., Mokarram Hossain, Konstantin Kikinov, Maximilian Kannapinn, Stephan Rudykh, and Antonio J. Gil (2026). “Neural networks meet hyperelasticity: A monotonic approach”. *European Journal of Mechanics - A/Solids* 116, p. 105900. ISSN: 0997-7538.
- Lee, Gisoo, Jaehee Lee, Seunghyeon Lee, Stephan Rudykh, and Hansohl Cho (2024a). “Extreme resilience and dissipation in heterogeneous elasto-plastomeric crystals”. *Soft Matter* 20.2, pp. 315–329.

- Lee, Jaehee, Jeongun Lee, Seounghee Yun, Sanha Kim, Howon Lee, Shawn A Chester, and Hansohl Cho (2024b). “Size-dependent fracture in elastomers: Experiments and continuum modeling”. *Physical Review Materials* 8.11, p. 115602.
- Lee, Jaehee, Seunghyeon Lee, Shawn A Chester, and Hansohl Cho (2023a). “Finite element implementation of a gradient-damage theory for fracture in elastomeric materials”. *International Journal of Solids and Structures* 279, p. 112309.
- Lee, Jaehee, David Veysset, Alex J Hsieh, Gregory C Rutledge, and Hansohl Cho (2023b). “A polyurethane-urea elastomer at low to extreme strain rates”. *International Journal of Solids and Structures* 280, p. 112360.
- Lei, Ming, Craig M Hamel, Chao Yuan, Haibao Lu, and H Jerry Qi (2018). “3D printed two-dimensional periodic structures with tailored in-plane dynamic responses and fracture behaviors”. *Composites Science and Technology* 159, pp. 189–198.
- Li, Jian, Viacheslav Slesarenko, Pavel I Galich, and Stephan Rudykh (2018). “Instabilities and pattern formations in 3D-printed deformable fiber composites”. *Composites Part B: Engineering* 148, pp. 114–122.
- Li, Tiantian, Fan Liu, and Lifeng Wang (2020). “Enhancing indentation and impact resistance in auxetic composite materials”. *Composites Part B: Engineering* 198, p. 108229.
- Li, Weichen, Yue Wang, Tian Chen, and Xiaojia Shelly Zhang (2023). “Algorithmic encoding of adaptive responses in temperature-sensing multimaterial architectures”. *Science Advances* 9.47, eadk0620.
- Li, Yaning, Narges Kaynia, Stephan Rudykh, and Mary C Boyce (2013). “Wrinkling of interfacial layers in stratified composites”. *Advanced Engineering Materials* 15.10, pp. 921–926.
- Ligon-Auer, Samuel Clark, Martin Schwentenwein, Christian Gorsche, Jürgen Stampfl, and Robert Liska (2016). “Toughening of photo-curable polymer networks: a review”. *Polymer Chemistry* 7.2, pp. 257–286.
- Liu, Fan, Tiantian Li, Xihang Jiang, Zian Jia, Zhiping Xu, and Lifeng Wang (2020). “The effect of material mixing on interfacial stiffness and strength of multi-material additive manufacturing”. *Additive Manufacturing* 36, p. 101502.
- Liu, Lei and Yaning Li (2018). “Failure mechanism transition of 3D-printed biomimetic sutures”. *Engineering Fracture Mechanics* 199, pp. 372–379.
- Lumpe, Thomas S, Jochen Mueller, and Kristina Shea (2019). “Tensile properties of multi-material interfaces in 3D printed parts”. *Materials & Design* 162, pp. 1–9.
- Mao, Yiqi, Zhen Ding, Chao Yuan, Shigang Ai, Michael Isakov, Jiangtao Wu, Tiejun Wang, Martin L Dunn, and H Jerry Qi (2016). “3D printed reversible shape changing components with stimuli responsive materials”. *Scientific reports* 6.1, p. 24761.
- Martin, John H, Brennan D Yahata, Jacob M Hundley, Justin A Mayer, Tobias A Schaedler, and Tresa M Pollock (2017). “3D printing of high-strength aluminium alloys”. *Nature* 549.7672, pp. 365–369.
- Meisel, Nicholas Alexander, David A Dillard, and Christopher B Williams (2018). “Impact of material concentration and distribution on composite parts manufactured via multi-material jetting”. *Rapid Prototyping Journal* 24.5, pp. 872–879.
- Mo, Chengyang, Yijie Jiang, and Jordan R Raney (2020). “Microstructural evolution and failure in short fiber soft composites: Experiments and modeling”. *Journal of the Mechanics and Physics of Solids* 141, p. 103973.

- Moon, Jehoon, Giso Lee, Jaehee Lee, and Hansoh Cho (2025). “Extreme resilience and dissipation in heterogeneous disordered materials”. *Journal of the Mechanics and Physics of Solids*, p. 106246.
- Moraleda, Joaquín, Javier Segurado, and Javier LLorca (2009). “Finite deformation of incompressible fiber-reinforced elastomers: a computational micromechanics approach”. *Journal of the Mechanics and Physics of Solids* 57.9, pp. 1596–1613.
- Mueller, Jochen, Diana Courty, Manuel Spielhofer, Ralph Spolenak, and Kristina Shea (2017). “Mechanical properties of interfaces in inkjet 3D printed single-and multi-material parts”. *3D Printing and Additive Manufacturing* 4.4, pp. 193–199.
- Narayan, Sooraj and Lallit Anand (2021). “Fracture of amorphous polymers: A gradient-damage theory”. *Journal of the Mechanics and Physics of Solids* 146, p. 104164.
- Nawafleh, Nashat and Emrah Celik (2020). “Additive manufacturing of short fiber reinforced thermoset composites with unprecedented mechanical performance”. *Additive Manufacturing* 33, p. 101109.
- Ortiz, Christine and Mary C Boyce (2008). “Bioinspired structural materials”. *Science* 319.5866, pp. 1053–1054.
- Park, Soyeon, Wan Shou, Liane Makatura, Wojciech Matusik, and Kun Kelvin Fu (2022). “3D printing of polymer composites: Materials, processes, and applications”. *Matter* 5.1, pp. 43–76.
- Qu, Meng, Fei Deng, Salmon M Kalkhoran, Andrew Gouldstone, Agathe Robisson, and Krystyn J Van Vliet (2011). “Nanoscale visualization and multiscale mechanical implications of bound rubber interphases in rubber–carbon black nanocomposites”. *Soft Matter* 7.3, pp. 1066–1077.
- Raney, Jordan R, Brett G Compton, Jochen Mueller, Thomas J Ober, Kristina Shea, and Jennifer A Lewis (2018). “Rotational 3D printing of damage-tolerant composites with programmable mechanics”. *Proceedings of the National Academy of Sciences* 115.6, pp. 1198–1203.
- Reyes-Martinez, Marcos A, Edwin P Chan, Christopher L Soles, Endao Han, Kieran A Murphy, Heinrich M Jaeger, Daniel R Reid, and Juan J de Pablo (2022). “Tuning the mechanical impedance of disordered networks for impact mitigation”. *Soft Matter* 18.10, pp. 2039–2045.
- Roach, Devin J, Craig M Hamel, Conner K Dunn, Marshall V Johnson, Xiao Kuang, and H Jerry Qi (2019). “The m4 3D printer: A multi-material multi-method additive manufacturing platform for future 3D printed structures”. *Additive Manufacturing* 29, p. 100819.
- Saadat, Fatemeh, Victor Birman, Stavros Thomopoulos, and Guy M Genin (2015). “Effective elastic properties of a composite containing multiple types of anisotropic ellipsoidal inclusions, with application to the attachment of tendon to bone”. *Journal of the Mechanics and Physics of Solids* 82, pp. 367–377.
- Sames, William J, FA List, Sreekanth Pannala, Ryan R Dehoff, and Sudarsanam Suresh Babu (2016). “The metallurgy and processing science of metal additive manufacturing”. *International materials reviews* 61.5, pp. 315–360.
- Sheng, Nuo, Mary C Boyce, David M Parks, GC Rutledge, JI Abes, and RE Cohen (2004). “Multiscale micromechanical modeling of polymer/clay nanocomposites and the effective clay particle”. *Polymer* 45.2, pp. 487–506.
- Sitthi-Amorn, Pitchaya, Javier E Ramos, Yuwang Wangy, Joyce Kwan, Justin Lan, Wenshou Wang, and Wojciech Matusik (2015). “MultiFab: a machine vision assisted platform for multi-material 3D printing”. *ACM Transactions on Graphics (Tog)* 34.4, pp. 1–11.

- Slesarenko, Viacheslav and Stephan Rudykh (2016). “Harnessing viscoelasticity and instabilities for tuning wavy patterns in soft layered composites”. *Soft Matter* 12.16, pp. 3677–3682.
- Slesarenko, Viacheslav and Stephan Rudykh (2017). “Microscopic and macroscopic instabilities in hyperelastic fiber composites”. *Journal of the Mechanics and Physics of Solids* 99, pp. 471–482.
- Slesarenko, Viacheslav and Stephan Rudykh (2018). “Towards mechanical characterization of soft digital materials for multimaterial 3D-printing”. *International Journal of Engineering Science* 123, pp. 62–72.
- Stratasys (2018). “Objet260 Connex 1/2/3”. URL: <https://support.stratasys.com/en/Printers/PolyJet-Legacy/Objet260-Connex-1-2-3>.
- Stratasys (2021). “Digital material (FLX2095-DM, FLX2070-DM)”. URL: <https://www.stratasys.com/en/materials/>.
- Stratasys (2025a). “TangoPlus (FLX930)”. URL: <https://www.stratasys.com/en/materials/>.
- Stratasys (2025b). “VeroBlackPlus (RGD875)”. URL: <https://www.stratasys.com/en/materials/>.
- Talamini, Brandon, Yunwei Mao, and Lallit Anand (2018). “Progressive damage and rupture in polymers”. *Journal of the Mechanics and Physics of Solids* 111, pp. 434–457.
- Telles, Rodrigo et al. (2025). “Spatially programmed alignment and actuation in printed liquid crystal elastomers”. *Proceedings of the National Academy of Sciences* 122.3, e2414960122.
- Wang, Yueping et al. (2017). “A biorobotic adhesive disc for underwater hitchhiking inspired by the remora suckerfish”. *Science Robotics* 2.10, eaan8072.
- Wu, Jiangtao, Chao Yuan, Zhen Ding, Michael Isakov, Yiqi Mao, Tiejun Wang, Martin L Dunn, and H Jerry Qi (2016). “Multi-shape active composites by 3D printing of digital shape memory polymers”. *Scientific reports* 6.1, p. 24224.
- Xiang, Yuhai, Danming Zhong, Peng Wang, Tenghao Yin, Haofei Zhou, Honghui Yu, Chinmay Baliga, Shaoxing Qu, and Wei Yang (2019). “A physically based visco-hyperelastic constitutive model for soft materials”. *Journal of the Mechanics and Physics of Solids* 128, pp. 208–218.
- Yang, Steven, Michal Levin, Govinda Anantha Padmanabha, Miriam Borshevsky, Ohad Cohen, D Thomas Seidl, Reese E Jones, Nikolaos Bouklas, and Noy Cohen (2025). “Physics augmented machine learning discovery of composition-dependent constitutive laws for 3D printed digital materials”. *International Journal of Engineering Science* 217, p. 104381.
- Yi, J, MC Boyce, GF Lee, and E Balizer (2006). “Large deformation rate-dependent stress–strain behavior of polyurea and polyurethanes”. *Polymer* 47.1, pp. 319–329.
- Zerhouni, O, MG Tarantino, and Kostas Danas (2019). “Numerically-aided 3D printed random isotropic porous materials approaching the Hashin-Shtrikman bounds”. *Composites Part B: Engineering* 156, pp. 344–354.
- Zhang, Pu and Albert C To (2016). “Transversely isotropic hyperelastic-viscoplastic model for glassy polymers with application to additive manufactured photopolymers”. *International Journal of Plasticity* 80, pp. 56–74.
- Zhao, Tuo, Xiangxin Dang, Konstantinos Manos, Shixi Zang, Jyotirmoy Mandal, Minjie Chen, and Glaucio H Paulino (2025). “Modular chiral origami metamaterials”. *Nature* 640.8060, pp. 931–940.
- Zhao, Yan, Jing Li, Yan Ping Cao, and Xi-Qiao Feng (2016). “Buckling of an elastic fiber with finite length in a soft matrix”. *Soft Matter* 12.7, pp. 2086–2094.

Zhu, Cheng, Hawi B Gemed, Eric B Duoss, and Christopher M Spadaccini (2024). "Toward multiscale, multi-material 3D printing". *Advanced Materials* 36.34, p. 2314204.

Zorzetto, Laura et al. (2020). "Properties and role of interfaces in multimaterial 3D printed composites". *Scientific reports* 10.1, p. 22285.